Taylor & Francis
Taylor & Francis Group

Combustion Theory and Modelling

ISSN: 1364-7830 (Print) 1741-3559 (Online) Journal homepage: http://www.tandfonline.com/loi/tctm20

A conservative, thermodynamically consistent numerical approach for low Mach number combustion. Part I: Single-level integration

Andrew Nonaka, Marcus S. Day & John B. Bell

To cite this article: Andrew Nonaka, Marcus S. Day & John B. Bell (2018) A conservative, thermodynamically consistent numerical approach for low Mach number combustion. Part I: Single-level integration, Combustion Theory and Modelling, 22:1, 156-184, DOI: 10.1080/13647830.2017.1390610

To link to this article: https://doi.org/10.1080/13647830.2017.1390610

Published online: 07 Nov 2017.

Combustion Theory and Modelling, 2018
Vol. 22, No. 1, 156–184, https://doi.org/10.1080/13647830.2017.1390610

A conservative, thermodynamically consistent numerical approach for low Mach number combustion. Part I: Single-level integration

Andrew Nonaka*, Marcus S. Day and John B. Bell

Center for Computational Sciences and Engineering, Lawrence Berkeley National Laboratory, Berkeley, USA

(*Received 25 April 2017; accepted 25 September 2017*)

We present a numerical approach for low Mach number combustion that conserves both mass and energy while remaining on the equation of state to a desired tolerance. We present both unconfined and confined cases, where in the latter the ambient pressure changes over time. Our overall scheme is a projection method for the velocity coupled to a multi-implicit spectral deferred corrections (SDC) approach to integrate the mass and energy equations. The iterative nature of SDC methods allows us to incorporate a series of pressure discrepancy corrections naturally that lead to additional mass and energy influx/outflux in each finite volume cell in order to satisfy the equation of state. The method is second order, and satisfies the equation of state to a desired tolerance with increasing iterations. Motivated by experimental results, we test our algorithm on hydrogen flames with detailed kinetics. We examine the morphology of thermodiffusively unstable cylindrical premixed flames in high-pressure environments for confined and unconfined cases. We also demonstrate that our algorithm maintains the equation of state for premixed methane flames and non-premixed dimethyl ether jet flames.

Keywords: low Mach number combustion; detailed chemistry and kinetics; thermodynamic pressure; confined domains; spectral deferred corrections

1. Introduction

Low Mach number numerical simulation methodology provides a valuable tool for efficiently modelling reacting flow with detailed kinetics and transport; see [1–8] for a variety of recent studies. Low Mach number models are derived from fully compressible equations using low Mach number asymptotics [9,10] and do not include acoustic wave propagation, allowing for much larger time steps based on an advective CFL condition. Central to the low Mach number approximation is a decomposition of the pressure into a background ambient pressure plus a perturbational pressure that is of the order of the Mach number squared. The ambient pressure represents the thermodynamic state of the fluid. The perturbational pressure does not affect the thermodynamic state of the fluid. Asymptotic analysis shows that, for small systems, the ambient pressure is spatially constant. For unconfined systems the ambient pressure is constant in time, whereas for confined systems the ambient pressure is a function of time that is determined by the thermodynamic processes within the domain. (We note that for large-scale atmospheric or stellar environments with density stratification, the ambient pressure can vary with height and time [11,12].)

*Corresponding author. Email: AJNonaka@lbl.gov

In the low Mach number system, the thermodynamic pressure is expressed in terms of the species masses and energy using an equation of state (EOS). The evolution of the mass and energy are constrained by the thermodynamic pressure, which ideally matches the ambient pressure. The perturbational pressure provides the mechanism for enforcing the constraint; it modifies the velocity field so that the combination of advection, diffusion, and reaction of the thermodynamic state leads to a thermodynamic pressure that matches the ambient pressure. Typically, in low Mach number systems, the constraint is recast as a divergence constraint on the velocity field, which is obtained by taking the Lagrangian derivative of the EOS. Analytically, this divergence constraint guarantees that the conservative evolution of mass and energy is thermodynamically consistent with the ambient pressure. However, in numerical simulations this is not true and the thermodynamic pressure will drift from the ambient pressure except in special cases (e.g. for a linear EOS). There are a number of choices for how to deal with this drift. One approach is to forego conservation and redefine either the mass or energy at the end of the integration step using the EOS and the ambient pressure. This approach has been used by many, and has been extended to adaptive meshes, and higher-order discretisations [13–18]. Another approach is to maintain conservation of mass and energy, and add a lagged correction term to the divergence constraint [19–21]. These methods have been referred to as 'volume discrepancy' approaches since they allow for additional mass and energy influx/outflux in each finite-volume cell to balance diffusion and reactions to maintain thermodynamic consistency. This correction term does not exactly preserve the EOS, but is able to control the drift to a modest degree.

In this paper, we will instead use the more suitable term 'pressure discrepancy' to refer to this lagged constraint correction. We present a new pressure discrepancy approach that iteratively modifies the constraint within a time step, so that we can reduce the thermodynamic drift to a desired tolerance while maintaining conservation of mass and energy. Our overall temporal integration strategy is based on second-order projection methodology [22,23] that extends Chorin's approach for incompressible flow [24]. The distinguishing feature of our algorithm is a new mass and energy integration scheme that uses multi-implicit spectral deferred corrections (SDC). SDC algorithms, originally introduced by Dutt *et al.* [25] for ordinary differential equations, are a class of numerical methods that represent the solution as an integral in time and iteratively solve a series of correction equations to reduce the error. Bourlioux, Layton and Minion [26,27] introduced a multi-implicit SDC approach for advection–diffusion–reaction systems where advection terms are evaluated explicitly, reaction and diffusion terms treated implicitly, and different time steps are used for each process. Recently, we introduced a multi-implicit SDC algorithm for low Mach number reacting flow [20] and demonstrated increased efficiency and accuracy over Strang splitting. In this approach, we used an explicit discretisation for advection, a semi-implicit discretisation for diffusion, and a variable-order BDF scheme (VODE) [28] for reactions. We have also developed a fourth-order one-dimensional multi-implicit SDC algorithm using a backward Euler discretisation for reactions that incorporates an iterative pressure discrepancy algorithm to reduce the thermodynamic drift [21].

In this paper, we present an improved version of the algorithm in [20], where we leverage the iterative nature of the scheme to compute a series of pressure discrepancy correction terms, where in each iteration we more accurately enforce the EOS. Two iterations are sufficient for second-order accuracy, but we demonstrate that we can reduce the thermodynamic drift to a desired tolerance with increasing iterations. We also present the modifications required for confined domains, where the ambient pressure is a function of time. A general prescription for modelling ambient pressure changes was presented in seminal works that derived the low Mach number equations [9,10]. Here, we propose an iterative pressure

discrepancy approach that allows us to update the ambient pressure iteratively while satisfying the EOS and preserving conservation. In the results section, we present convergence results for hydrogen flames as a function of SDC iterations, and examine the thermodynamic drift as a function of SDC iteration. We also demonstrate the performance of our code on a thermodiffusively unstable configuration (cylindrical premixed hydrogen flames). Next we compare our results to our previous methane flame calculations [20], and finally, we demonstrate our capability for simulating non-premixed dimethyl ether jet flames in two dimensions.

2. Model equations

In the low Mach number regime, the characteristic fluid velocity is small compared to the sound speed (typically the Mach number is $M = U/c \sim \mathcal{O}(0.1)$ or smaller), and the effect of acoustic wave propagation is unimportant to the overall dynamics of the system. In a low Mach number numerical method, acoustic wave propagation is mathematically removed from the equations of motion, allowing for a time step based on an advective CFL condition. Thus, this approach leads to a $\sim 1/M$ increase in the allowable time step over an explicit compressible approach (if the time step is limited by advective transport). Note that a low Mach number method does not enforce that the Mach number remain small, but rather is suitable for flows in this regime.

In this paper, we use the low Mach number equation set from [19,20], which is based on the model for low Mach number combustion introduced by Rehm and Baum [9] and rigorously derived from an asymptotic analysis by Majda and Sethian [10]. We consider a gaseous mixture ignoring Soret and Dufour effects, and assume a mixture model for species diffusion [29,30]. The resulting equations are a set of partial differential equations for mass, momentum, and energy representing coupled advection, diffusion, and reaction processes that are closed by an EOS (here we use an ideal gas). We note that the ideal gas assumption is not central to the success of the method we propose, but does allow us to express the algorithm and subsequent examples more concretely.

Fundamental to the low Mach number approach is that we can decompose the total pressure as

$$p(\mathbf{x}, t) = p_0(t) + \pi(\mathbf{x}, t), \tag{1}$$

where p_0 is the ambient pressure and π is a perturbational pressure field satisfying $\pi / p_0 \sim \mathcal{O}(M^2)$. The evolution of the system is constrained so that the thermodynamic state of the fluid is consistent with the ambient pressure p_0. The perturbational pressure π controls the evolution of the velocity to preserve spatial homogeneity of the thermodynamic state of the fluid.

Using the notation in [19,20], the evolution equations for the thermodynamic variables, $(\rho, \mathbf{Y}, h)$, are instantiations of mass and energy conservation:

$$\frac{\partial(\rho Y_m)}{\partial t} = -\nabla \cdot (\mathbf{U}\rho Y_m) - \nabla \cdot \mathbf{\Gamma}_m + \dot{\omega}_m, \tag{2}$$

$$\frac{\partial(\rho h)}{\partial t} = -\nabla \cdot (\mathbf{U}\rho h) + \frac{Dp_0}{Dt} + \nabla \cdot \frac{\lambda}{c_p}\nabla h + \sum_m \nabla \cdot h_m \left(\rho \mathcal{D}_m - \frac{\lambda}{c_p}\right) \nabla Y_m, \tag{3}$$

where ρ is the density, Y_m is the species m mass fraction with $\mathbf{Y}$ the vector of all mass fractions, $\mathcal{D}_m(\mathbf{Y}, T)$ are the species mixture-averaged diffusion coefficients, $\mathbf{\Gamma}_m \equiv -\rho\mathcal{D}_m\nabla Y_m$ are the species diffusion fluxes, $T = T(\rho, \mathbf{Y}, h)$ is the temperature, $\dot{\omega}_m(\mathbf{Y}, T)$ is the production rate for ρY_m due to chemical reactions, $h = \sum_m Y_m h_m$ is the enthalpy with $h_m = h_m(T)$ the enthalpy of species m, $\lambda(\mathbf{Y}, T)$ is the thermal conductivity, and $c_p = \sum_m Y_m \mathrm{d}h_m/\mathrm{d}T$ is the specific heat at constant pressure. Our definition of enthalpy includes the standard enthalpy of formation, so there is no net change to h due to reactions. Summing the species equations and noting that $\sum_m Y_m = 1$ and $\sum_m \dot{\omega}_m = 0$, we see that (2) implies the continuity equation,

$$\frac{\partial \rho}{\partial t} = -\nabla \cdot (\mathbf{U}\rho). \tag{4}$$

A property of multicomponent diffusive transport is that the species diffusion fluxes, $\mathbf{\Gamma}_m$, must sum to zero in order to conserve total mass. For mixture models such as the one considered here, that property is not satisfied in general. To conserve mass, these fluxes must be modified so that they sum to zero. We use the 'conservation diffusion velocity' approach described in [19] to correct $\mathbf{\Gamma}_m$. Also, whenever $\mathbf{\Gamma}_m$ is evaluated implicitly (as is done in the implicit diffusion discretisations for Y_m), we first solve the implicit system, conservatively correct $\mathbf{\Gamma}_m$, and then modify the time-advanced values of Y_m to be consistent with the corrected fluxes. These modifications will be noted in the algorithm descriptions below.

The evolution equation for velocity is a form of conservation of momentum:

$$\rho\left(\frac{\partial \mathbf{U}}{\partial t} + \mathbf{U}\cdot\nabla\mathbf{U}\right) = -\nabla\pi + \nabla\cdot\boldsymbol{\tau}, \tag{5}$$

with stress tensor

$$\boldsymbol{\tau} = \mu\left[\nabla\mathbf{U} + (\nabla\mathbf{U})^{\mathrm{T}} - \frac{2}{3}\mathcal{I}(\nabla\cdot\mathbf{U})\right], \tag{6}$$

where $\mu(\mathbf{Y}, T)$ is the viscosity and $\mathcal{I}$ is the identity tensor.

The system is closed by specifying the EOS. Here we use the ideal gas EOS,

$$p_{\mathrm{therm}} = \rho\mathcal{R}T\sum_m \frac{Y_m}{W_m}, \tag{7}$$

where $\mathcal{R}$ is the universal gas constant and W_m is the molecular weight of species m. In the low Mach number model, the thermodynamic pressure computed from the species masses and the energy using the EOS, p_{therm}, ideally is equal to the prescribed ambient pressure, p_0.

Equations (2), (3), and (5) all subject to (7) (with p_0 instead of p_{therm}) form the system that we would like to solve. Rather than directly attacking this system of constrained differential algebraic equations, we use a standard approach of recasting the EOS (7) as a divergence constraint on the velocity field. To do this, we differentiate the EOS in the

Lagrangian frame of the moving fluid,

$$\frac{\mathrm{D}p}{\mathrm{D}t} = \frac{\partial p}{\partial \rho}\frac{\mathrm{D}\rho}{\mathrm{D}t} + \frac{\partial p}{\partial T}\frac{\mathrm{D}T}{\mathrm{D}t} + \sum_m \frac{\partial p}{\partial Y_m}\frac{\mathrm{D}Y_m}{\mathrm{D}t}. \tag{8}$$

Using continuity (4), taking the partial derivatives of (7) and rearranging terms, we rewrite (8) as

$$\nabla \cdot \mathbf{U} = \left(-\frac{1}{p}\frac{\mathrm{D}p}{\mathrm{D}t} + \frac{1}{T}\frac{\mathrm{D}T}{\mathrm{D}t} + \frac{W}{W_m}\frac{\mathrm{D}Y_m}{\mathrm{D}t} \right), \tag{9}$$

where $W = (\sum_m Y_m/W_m)^{-1}$ is the mixture-averaged molecular weight. For open domains we replace p with the constant ambient pressure, p_0. Next, we substitute in the evolution equations for temperature (converted from the enthalpy equation; see Equation (12) in [19]), and species (2) to obtain the constraint

$$\begin{aligned} \nabla \cdot \mathbf{U} = {} & \frac{1}{\rho c_p T}\left(\nabla \cdot \lambda \nabla T - \sum_m \mathbf{\Gamma}_m \cdot \nabla h_m \right) \\ & - \frac{1}{\rho}\sum_m \frac{W}{W_m} \nabla \cdot \mathbf{\Gamma}_m + \frac{1}{\rho}\sum_m \left(\frac{W}{W_m} - \frac{h_m}{c_p T} \right) \dot{\omega}_m \equiv S. \end{aligned} \tag{10}$$

Altogether, this approach leads to instantaneous acoustic equilibration while retaining local compressibility effects due to reactions, mass diffusion, and thermal diffusion. Analytically, this velocity field guarantees that the conservative evolution of mass and energy is thermodynamically consistent with the ambient pressure.

3. Pressure discrepancy

In our time-advancement scheme, as part of the computation of the advective fluxes for mass and energy, we apply a projection operator to compute advection velocities at cell faces that discretely satisfy the divergence constraint (10). In our derivation of the constraint, we reformulated (8) as (9) by substituting in the evolution equations for temperature, species, and density while assuming the pressure to be constant. Thus, the resulting velocity field corresponds analytically to the velocity required so that the advective fluxes of mass and energy lead to constant thermodynamic pressure. Numerically this is not the case, and the solution drifts from the EOS. The key observation in pressure discrepancy approaches is that we can replace the derivative of pressure in (9) with local numerical values that specify how we wish the local thermodynamic pressure to change over a time step to account for the numerical drift. After numerical integration over a time step, for a given cell if the thermodynamic pressure is too low, the net flux into the cell needs to be increased; if it is too high, the net flux needs to be decreased.

Before proceeding to the iterative scheme, it is important to note that, in general, the mass and energy are not in thermodynamic equilibrium at the beginning of a time step, so we define a correction term, χ, to the right-hand side of the velocity constraint based on the local corrections required in each cell to be used in the first SDC iteration,

$$\chi = \frac{1}{p^n_{\mathrm{therm}}}\frac{p^n_{\mathrm{therm}} - p_0}{\Delta t}. \tag{11}$$

Again, this correction can be derived by considering (9) and the fact that we are adding an additional term to the right-hand side with the intent of changing the thermodynamic pressure locally in each cell. We note that for a general EOS, the correction term has the form

$$\chi = \frac{1}{\rho p_\rho} \frac{p^n_{\text{therm}} - p_0}{\Delta t}, \quad p_\rho = \left.\frac{\partial p}{\partial \rho}\right|_{\mathbf{Y},T}. \tag{12}$$

Next we perform a series of SDC correction steps, each iteratively updating the time-advanced solution. At the end of each SDC iteration, we increment χ based on the latest thermodynamic pressure, where the superscript (k) denotes the time-advanced solution after the kth SDC iterate,

$$\chi := \chi + \frac{1}{p^{(k)}_{\text{therm}}} \frac{p^{(k)}_{\text{therm}} - p_0}{\Delta t}. \tag{13}$$

This correction term is used in the projection operator to compute the updated advection velocities in the next iteration.

In our previous work [20], we only included the initial pressure discrepancy correction using the state at t^n and did not iteratively modify χ. We also made the design decision to fix the advection velocities, i.e. we did not recompute the advection velocities with each iteration. Here, we modify χ with each SDC iteration and apply the projection operator to compute updated advection velocities, which effectively drives the deviation of the thermodynamic pressure from the ambient pressure to zero with increasing iteration count. A similar technique is used in our fourth-order approach for one-dimensional low Mach number combustion [21]. The full implementation details for our scheme are given in Section 5.

4. Confined domain ambient pressure

In our previous work, we have considered unconfined domains where the ambient pressure is constant in time. For confined domain systems this is not the case. The mathematical formulation describing how the ambient pressure evolves over time was originally derived in [9,10]. Here we summarise these results, and describe how to incorporate a pressure discrepancy approach so that the thermodynamic variables evolve in a consistent manner. In the derivation of (10) we assumed p_0 was constant. If p_0 is a function of time, we restore the pressure derivative term so the constraint becomes

$$\nabla \cdot \mathbf{U} + \theta \frac{\mathrm{d}p_0}{\mathrm{d}t} = S, \tag{14}$$

where $\theta \equiv 1/(\Gamma_1 p_0)$, with $\Gamma_1 = \partial \ln(p)/\partial \ln(\rho)|_s$ being the first adiabatic exponent. We note that here, unlike in the work of Majda and Sethian [10], Γ_1 depends on composition and is not a constant. A detailed derivation of θ can be found in Appendix A of [31]. The unknowns in (14) are $\mathbf{U}$ and $\mathrm{d}p_0/\mathrm{d}t$. We can rewrite this equation as follows:

$$\nabla \cdot \mathbf{U} + (\bar{\theta} + \delta\theta)\frac{\mathrm{d}p_0}{\mathrm{d}t} = \bar{S} + \delta S, \tag{15}$$

where $\bar{\theta}$ and $\bar{S}$ are the mean values of θ and S over the domain, and $\delta\theta$ and δS are perturbations off the mean that, by definition, integrate to zero over the domain. Thus, $S = \bar{S} + \delta S$ and $\theta = \bar{\theta} + \delta\theta$. By the divergence theorem $\int \nabla \cdot \mathbf{U}\, \mathrm{d}V = 0$ in a closed domain, since the normal velocity is equal to zero on the entire domain boundary. Furthermore, p_0 is only a function of time. These observations allow us to decompose changes in the thermodynamic state into an evolution equation for p_0,

$$\bar{\theta}\frac{\mathrm{d}p_0}{\mathrm{d}t} = \bar{S}, \tag{16}$$

and a velocity constraint,

$$\nabla \cdot \mathbf{U} = \delta S - \delta\theta\frac{\mathrm{d}p_0}{\mathrm{d}t} \tag{17}$$

$$= \delta S - \delta\theta\frac{\bar{S}}{\bar{\theta}}. \tag{18}$$

We can again use χ to remain on the equation of state, but we need to split $\chi = \bar{\chi} + \delta\chi$ into mean and perturbational components in order to form a solvable system for $\mathrm{d}p_0/\mathrm{d}t$ and $\mathbf{U}$. The full details are described in the time-advancement scheme below.

5. Numerical algorithm

Our overall temporal integration strategy uses the projection method framework discussed in Day and Bell [19], which is based on second-order extensions [22,23] of Chorin's algorithm for incompressible flow [24]. We use an explicit discretisation for the convective terms and a semi-implicit treatment of momentum diffusion to create a provisional update to the velocity field. The velocity field is projected onto the space satisfying the divergence condition (10) for open domains or (18) for closed domains while simultaneously updating the perturbational pressure, π. Within this framework, we incorporate a new temporal integration scheme for the mass and energy. Our approach is based on the multi-implicit SDC approach originally presented in [26,27] for reacting gas dynamics, and later extended to low Mach number combustion in [20]. We refer the reader to Sections 3.1 and 3.2 in [20] for an overview on SDC methods, and on how the multi-implicit formulation can be applied to the mass and energy evolution. To summarise, we couple advection, diffusion, and reaction by iteratively re-integrating each physical process using lagged source terms representing the effects of the other physical processes. We use a second-order explicit Godunov scheme for advection, a semi-implicit discretisation of diffusion, and a high-order stiff chemical kinetics solver (VODE) [28] for reactions. The source terms are carefully constructed in a way that reduces splitting error as the number of iterations increases.

The algorithm in this paper differs from [20] in three ways. The first change is that, rather than performing a predictor and a series of corrector steps, we have re-factored our algorithm to require only a series of notationally identical corrector steps. This is a simplification of the algorithm that still preserves the convergence properties of SDC methods. Second, our pressure discrepancy approach for maintaining the equation of state requires iteratively recomputing the advective velocities used to construct mass and energy fluxes, as outlined in Section 3. Third, we present the modifications required to track the ambient pressure change while maintaining the equation of state for confined domains, as outlined in Section 4.

We use a finite-volume, Cartesian grid approach with constant grid spacing, where $\mathbf{U}$, ρ, $\mathbf{Y}$, h, and T represent cell averages at integer indexed time levels t^n, whereas π is defined at nodal point-values at half time levels, $t^{n-1/2}$. We wish to advance the species (2), enthalpy (3), and momentum (5) in time subject to constraint (10). The thermodynamic variable advance is a series of SDC corrector steps. We use the superscript '(k)' notation to denote the time-advanced solution at t^{n+1} after the kth iterate. When we denote the right-hand side of the constraint, S, and also transport coefficients with a superscript 'n', '(k)', '$n+1$', etc., it is understood that they are computed directly from the corresponding thermodynamic variables.

Given the complete state at t^n (and pressure $\pi^{n-1/2}$), the steps to advance the solution by Δt to t^{n+1} are as follows.

Step 1: (*Compute unconstrained advection velocities*) Use a second-order Godunov procedure to predict a time-centred velocity, $\mathbf{U}^{\mathrm{ADV},*}$, on cell faces. This procedure is identical to the algorithm described in detail in Section 2.1 of [32] for computing normal velocities on cell faces. The provisional field, $\mathbf{U}^{\mathrm{ADV},*}$, represents a normal velocity on cell faces analogous to a MAC-type staggered grid discretisation of the Navier–Stokes equations (see [33], for example). However, $\mathbf{U}^{\mathrm{ADV},*}$ fails to satisfy the divergence constraint (10).

Step 2: (*Initialise time-advanced thermodynamic variables*) We set the initial estimate for the thermodynamic variables at t^{n+1} equal to the state at t^n, i.e. $(\rho h,\ \rho\mathbf{Y})^{(k=0)} = (\rho h,\ \rho\mathbf{Y})^n$. Also, we set the first estimate for the updated ambient pressure in the same way, $p_0^{(k=0)} = p_0^n$. We will loop over **Steps 3** and **4** to update this estimate iteratively. We also initialise the pressure discrepancy correction to $\chi^{n+1/2,(k=0)} = 0$ and will increment this correction term iteratively.

Next, we loop over **Step 3** and **Step 4** from $k = 1, k_{\max}$ as follows.

Step 3: (*Compute constrained advection velocities*) Update χ using the current estimate for the time-advanced state,

$$\chi^{n+1/2,(k)} = \chi^{n+1/2,(k-1)} + \frac{1}{p_{\mathrm{therm}}^{(k-1)}} \frac{p_{\mathrm{therm}}^{(k-1)} - p_0^{(k-1)}}{\Delta t}. \tag{19}$$

Again, note that in the first iteration ($k = 1$), all quantities with a $(k-1)$ superscript are copies of the state from t^n. Next we define a time-centred right-hand side for the constraint equation (noting that we include χ in the right-hand side) along with a time-centred θ,

$$S^{n+1/2,(k)} = \left(\frac{S^n + S^{(k-1)}}{2} + \chi^{n+1/2,(k)} \right), \tag{20}$$

$$\theta^{n+1/2,(k)} = \frac{\theta^n + \theta^{(k-1)}}{2}. \tag{21}$$

We want to solve the following constraint equation for the velocity and the time-derivative of the ambient pressure:

$$\nabla \cdot \mathbf{U}^{\mathrm{ADV},(k)} + \theta^{n+1/2,(k)} \left(\frac{\mathrm{d}p_0}{\mathrm{d}t} \right)^{n+1/2,(k)} = S^{n+1/2,(k)}. \tag{22}$$

For unconfined domains, we set $(\mathrm{d}p_0/\mathrm{d}t)^{n+1/2,(k)} = 0$, and define $S_{\mathrm{eff}}^{n+1/2,(k)} = S^{n+1/2,(k)}$. For confined domains, we split θ and S into average and perturbational quantities:

$$\nabla \cdot \mathbf{U}^{\mathrm{ADV},(k)} + (\bar{\theta}^{n+1/2,(k)} + \delta\theta^{n+1/2,(k)}) \left(\frac{\mathrm{d}p_0}{\mathrm{d}t} \right)^{n+1/2,(k)} = \bar{S}^{n+1/2,(k)} + \delta S^{n+1/2,(k)}. \tag{23}$$

In order for this system to be solvable, we set the spatially constant terms equal to each other,

$$\left(\frac{\mathrm{d}p_0}{\mathrm{d}t} \right)^{n+1/2,(k)} = \frac{\bar{S}^{n+1/2,(k)}}{\bar{\theta}^{n+1/2,(k)}}, \tag{24}$$

and define a pressure update using this derivative,

$$p_0^{(k)} = p_0^n + \Delta t \left(\frac{\mathrm{d}p_0}{\mathrm{d}t} \right)^{n+1/2,(k)}. \tag{25}$$

The velocity is now subject to the following constraint, noting that by construction the terms on the right-hand side integrate to zero over the domain:

$$\nabla \cdot \mathbf{U}^{\mathrm{ADV},(k)} = \delta S^{n+1/2,(k)} - \delta\theta^{n+1/2,(k)} \left(\frac{\mathrm{d}p_0}{\mathrm{d}t} \right)^{n+1/2,(k)} \equiv S_{\mathrm{eff}}^{n+1/2,(k)}. \tag{26}$$

For both confined and unconfined domains, we apply a discrete projection by first solving the elliptic equation

$$D^{\mathrm{F}\to\mathrm{C}} \frac{1}{\rho^n} G^{\mathrm{C}\to\mathrm{F}} \phi^{(k)} = D^{\mathrm{F}\to\mathrm{C}} \mathbf{U}^{\mathrm{ADV},*} - S_{\mathrm{eff}}^{n+1/2,(k)} \tag{27}$$

for a cell-averaged $\phi^{(k)}$, where $D^{\mathrm{F}\to\mathrm{C}}$ represents a cell-averaged divergence of face-averaged data, and $G^{\mathrm{C}\to\mathrm{F}}$ represents a face-averaged gradient of cell-averaged data, and ρ^n is computed on cell faces using arithmetic averaging from neighbouring cells. The solution, $\phi^{(k)}$, is then used to define face-centred velocities that satisfy the constraint

$$\mathbf{U}^{\mathrm{ADV},(k)} = \mathbf{U}^{\mathrm{ADV},*} - \frac{1}{\rho^n} G^{\mathrm{C}\to\mathrm{F}} \phi^{(k)}. \tag{28}$$

Thus, $\mathbf{U}^{\mathrm{ADV},(k)}$ is a second-order accurate, staggered grid vector field at $t^{n+1/2}$ that discretely satisfies the constraint (10), and is used for computing the time-explicit advective fluxes for ρh, and $\rho\mathbf{Y}$, and time-explicit convective term for $\mathbf{U}$.

For notational simplicity, in **Step 4** we will refer to $\mathbf{U}^{\mathrm{ADV},(k)}$ and $(\mathrm{d}p_0/\mathrm{d}t)^{n+1/2,(k)}$ as $\mathbf{U}^{\mathrm{ADV}}$ and $(\mathrm{d}p_0/\mathrm{d}t)^{n+1/2}$. Note that, as we iterate over **Step 3** and **Step 4**, the numerical values of these fields are updated in each iteration.

Step 4: (*Advance thermodynamic variables*) There are several sub-steps involved in integrating $(\rho\mathbf{Y}, \rho h)$ over the full time step to obtain an updated estimate of the time-advanced state.

Step 4a: (*Advection step*) We use a standard unsplit multidimensional Godunov scheme [34,35] using upwinding based on the constrained MAC velocity field, $\mathbf{U}^{\mathrm{ADV}}$, to compute face-centred, time-centred edge states for mass and energy, $(\rho\mathbf{Y}, \rho h)^{n+1/2}$. This procedure is also described in detail in Section 2.1 of [32]. Note that the equations of motion (2) and (3) have the general form

$$\frac{\partial(\rho Y_m)}{\partial t} + \nabla\cdot(\mathbf{U}\rho Y_m) = \mathcal{R}_{\rho Y_m} \tag{29}$$

$$\frac{\partial(\rho h)}{\partial t} + \nabla\cdot(\mathbf{U}\rho h) = \mathcal{R}_{\rho h}. \tag{30}$$

In the Godunov scheme, the forcing terms, $\mathcal{R}_{\rho Y_m}$ and $\mathcal{R}_{\rho h}$, are explicitly evaluated from the t^n state, except for the time derivative of the ambient pressure, where we use (24), and for the reaction term in the mass equations, where we use lagged estimates of the integral of $\dot{\omega}_m$ over the time step.

The face-centred, time-centred velocities and scalars are used to construct advective flux divergences that are used in subsequent steps to solve for mass and enthalpy diffusion implicitly, as well as part of the source term in the reaction integration.

Since $\rho^{n+1/2} = \sum_m (\rho Y_m)^{n+1/2}$, we can now integrate total density over Δt to advance ρ^n to $\rho^{(k)}$ using

$$\rho^{(k)} = \rho^n - \Delta t\nabla\cdot(\mathbf{U}^{\mathrm{ADV}}\rho^{n+1/2}). \tag{31}$$

Step 4b: (*Mass diffusion correction equation*) Compute conservatively corrected versions of $\mathbf{\Gamma}_m^{(k-1)} = -\rho^{(k-1)}\mathcal{D}_m^{(k-1)}\nabla Y_m^{(k-1)}$. Then, following the multi-implicit SDC approach, compute provisional, time-advanced species mass fractions, $Y_{m,\mathrm{AD}}^{(k)}$, by solving a backward Euler type correction equation:

$$\begin{aligned}\frac{\rho^{(k)}Y_{m,\mathrm{AD}}^{(k)} - (\rho Y_m)^n}{\Delta t} &= -\nabla\cdot\left(\mathbf{U}^{\mathrm{ADV}}(\rho Y_m)^{n+1/2}\right)\\ &+\nabla\cdot\rho^{(k-1)}\mathcal{D}_m^{(k-1)}\nabla Y_{m,\mathrm{AD}}^{(k)} - \frac{1}{2}\nabla\cdot\left(\mathbf{\Gamma}_m^n - \mathbf{\Gamma}_m^{(k-1)}\right) + I_{R,\rho Y_m}^{(k-1)}.\end{aligned} \tag{32}$$

Note that $I_{R,\rho Y_m}^{(k-1)}$ is the effect of the chemistry, defined iteratively in Equation (37). In the first SDC iteration, we use the final value from the previous time step. Each of the species equations is implicit, requiring a linear solve for $Y_{m,\mathrm{AD}}^{(k)}$.

Next, compute conservatively corrected versions of iteratively-lagged species fluxes, $\mathbf{\Gamma}_{m,\mathrm{AD}}^{(k)} = -\rho^{(k-1)}\mathcal{D}_m^{(k-1)}\nabla Y_{m,\mathrm{AD}}^{(k)}$ and define an effective contribution of

advection–diffusion to the update of ρY_m:

$$Q^{(k)}_{\rho Y_m} = -\nabla \cdot \left(\mathbf{U}^{\mathrm{ADV}} (\rho Y_m)^{n+1/2} \right) - \nabla \cdot \mathbf{\Gamma}^{(k)}_{m,\mathrm{AD}} - \frac{1}{2} \nabla \cdot \left(\mathbf{\Gamma}^{n}_{m} - \mathbf{\Gamma}^{(k-1)}_{m} \right). \quad (33)$$

Step 4c: (*Enthalpy diffusion correction equation*) Following the multi-implicit SDC approach, compute a provisional, time-advanced enthalpy, $h^{(k)}_{\mathrm{AD}}$, by solving a backward Euler type correction equation:

$$\begin{aligned} \frac{\rho^{(k)} h^{(k)}_{\mathrm{AD}} - (\rho h)^n}{\Delta t} &= -\nabla \cdot \left(\mathbf{U}^{\mathrm{ADV}} (\rho h)^{n+1/2} \right) + \left(\frac{\mathrm{d}p_0}{\mathrm{d}t} \right)^{n+1/2} \\ &+ \nabla \cdot \frac{\lambda^{(k-1)}}{c_p^{(k-1)}} \nabla h^{(k)}_{\mathrm{AD}} + \frac{1}{2} \left(\nabla \cdot \frac{\lambda^n}{c_p^n} \nabla h^n - \nabla \cdot \frac{\lambda^{(k-1)}}{c_p^{(k-1)}} \nabla h^{(k-1)} \right) \\ &- \frac{1}{2} \sum_m \nabla \cdot \left[h^n_m \left(\mathbf{\Gamma}^n_m + \frac{\lambda^n}{c_p^n} \nabla Y^n_m \right) + h^{(k-1)}_m \left(\mathbf{\Gamma}^{(k-1)}_m + \frac{\lambda^{(k-1)}}{c_p^{(k-1)}} \nabla Y^{(k-1)}_m \right) \right]. \end{aligned} \quad (34)$$

The enthalpy term is implicit, requiring a linear solve for $h^{(k)}_{\mathrm{AD}}$, whereas the species enthalpy terms, h_m, are discretised with a trapezoidal rule using iteratively lagged, time-advanced values of h_m in order to avoid a more computationally expensive linear system. Once we have computed $h^{(k)}_{\mathrm{AD}}$, we define $Q^{(k)}_{\rho h}$ as the evaluation of the right-hand side of (34), which represents an effective contribution of advection–diffusion to the update of ρh.

Step 4d: (*Chemistry integration*) Use the VODE [28] package to integrate species (2) and enthalpy (3) over Δt to advance $(\rho \mathbf{Y}, \rho h)^n$ to $(\rho \mathbf{Y}, \rho h)^{(k)}$ using the advection/diffusion source terms, $Q^{(k)}_{\rho Y_m}$ and $Q^{(k)}_{\rho h}$ (defined in **Steps 4b** and **4c**):

$$\frac{\partial (\rho Y_m)}{\partial t} = Q^{(k)}_{\rho Y_m} + \dot{\omega}_m(\mathbf{Y}, T), \quad (35)$$

$$\frac{\partial (\rho h)}{\partial t} = Q^{(k)}_{\rho h}. \quad (36)$$

The SDC iterations are designed so that, upon convergence, the burning will be consistent with a time-varying, spatially uniform pressure. The burning is performed in a manner consistent with a time-varying, spatially uniform thermodynamic pressure. After the integration is complete, we compute the effect of reactions in the evolution of ρY_m in the VODE integration by defining

$$I^{(k)}_{R,\rho Y_m} = \frac{(\rho Y_m)^{(k)} - (\rho Y_m)^n}{\Delta t} - Q^{(k)}_{\rho Y_m}. \quad (37)$$

If $k < k_{\max}$, set $k = k + 1$ and return to **Step 3**. Otherwise, the time-advancement of the thermodynamic variables is complete, and set the new-time thermodynamic variables using $(\rho \mathbf{Y}, \rho h, p_0)^{n+1} = (\rho \mathbf{Y}, \rho h, p_0)^{(k_{\max})}$.

Step 5: (*Advance the velocity*) Next, we compute a provisional time-advanced, cell-averaged velocity field, $\mathbf{U}^{n+1,*}$ using the lagged pressure gradient, by solving

$$\frac{\mathbf{U}^{n+1,*}-\mathbf{U}^{n}}{\Delta t} = -\nabla\cdot\left(\mathbf{U}^{\mathrm{ADV}}\mathbf{U}^{n+1/2}\right) + \mathbf{U}^{n+1/2}\nabla\cdot\mathbf{U}^{\mathrm{ADV}} + \frac{1}{2\rho^{n+1/2}}\left(\nabla\cdot\boldsymbol{\tau}^{n}+\nabla\cdot\boldsymbol{\tau}^{n+1,*}\right) - \frac{1}{\rho^{n+1/2}}\nabla\pi^{n-1/2}, \quad (38)$$

where $\boldsymbol{\tau}^{n+1,*} = \mu^{n+1}[\nabla\mathbf{U}^{n+1,*} + (\nabla\mathbf{U}^{n+1,*})^{\mathrm{T}} - 2/3\,\mathcal{I}S^{n+1}]$ and $\rho^{n+1/2} = (\rho^{n} + \rho^{n+1})/2$. This is a semi-implicit discretisation for $\mathbf{U}^{n+1,*}$, requiring a linear solve. The face-centred, time-centred velocity in the convective term, $\mathbf{U}^{n+1/2}$, is computed using the same Godunov procedure used to compute $(\rho\mathbf{Y}, \rho h)^{n+1/2}$. Note that we are discretising (5) in conservative form so we can use multilevel synchronisation strategies for future adaptive mesh refinement (AMR) simulations that rely on tracking fluxes across coarse–fine interfaces [19,32,36]. The extension of this algorithm to AMR will be addressed in future work.

At this point, the intermediate cell-centred, new-time velocity field $\mathbf{U}^{n+1,*}$ does not satisfy the constraint (10). Hence, we apply an approximate projection to decompose $\mathbf{U}^{n+1,*}$ into an update of the perturbational pressure field and the final new-time velocity, $\mathbf{U}^{n+1}$. In particular, we solve

$$L^{\mathrm{N}\to\mathrm{N}}\phi^{\mathrm{N}} = D^{\mathrm{C}\to\mathrm{N}}\left(\mathbf{U}^{n+1,*} + \frac{\Delta t}{\rho^{n+1/2}}G^{\mathrm{N}\to\mathrm{C}}\pi^{n-1/2}\right) - S_{\mathrm{eff}}^{n+1} \quad (39)$$

for nodal values of ϕ^{N}. Here, $L^{\mathrm{N}\to\mathrm{N}}$ represents a nodal Laplacian of nodal data, computed using the standard bilinear finite-element approximation to $\nabla\cdot(1/\rho^{n+1/2})\nabla$. Also, $D^{\mathrm{C}\to\mathrm{N}}$ is a discrete second-order operator that approximates the divergence at nodes from cell-averaged data and $G^{\mathrm{N}\to\mathrm{C}}$ approximates a cell-averaged gradient from nodal data. For open chambers, $S_{\mathrm{eff}}^{n+1} = S^{n+1}$. For closed chambers, we do not need to compute an update to p_0 in this step since we have already computed a new ambient pressure that is consistent with thermodynamic processes. In order to address solvability issues, following our splitting of θ and S into average and perturbational quantities used in the MAC projection (see Equation 18), we have

$$S_{\mathrm{eff}}^{n+1} = \delta S^{n+1} - \delta\theta^{n+1}\frac{\bar{S}^{n+1}}{\bar{\theta}^{n+1}}. \quad (40)$$

Also note that there is no χ correction in this projection since these velocities are not directly used to compute the advection terms for the thermodynamic variables. Equation (39) requires nodal values of S_{eff}^{n+1}, which we obtain by averaging the neighbouring cell-averaged values. Finally, we determine the new-time cell-averaged velocity field using

$$\mathbf{U}^{n+1} = \mathbf{U}^{n+1,*} - \frac{\Delta t}{\rho^{n+1/2}}G^{\mathrm{N}\to\mathrm{C}}(\phi^{\mathrm{N}} - \pi^{n-1/2}) \quad (41)$$

and the new time-centred pressure using $\pi^{n+1/2} = \phi^{\mathrm{N}}$. This completes the description of the time-advancement algorithm.

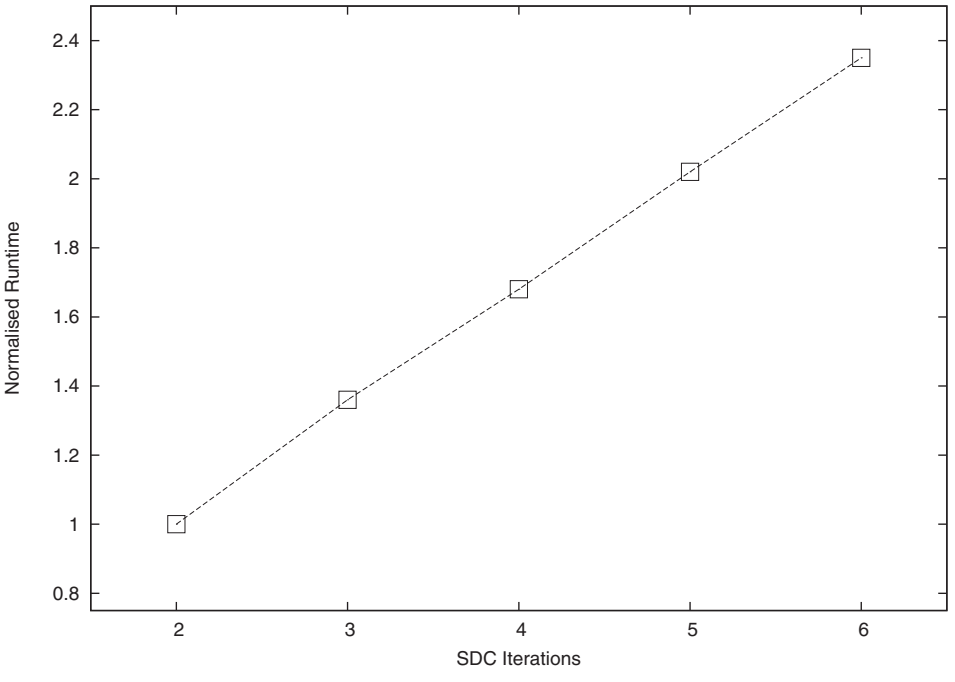

Figure 1. Normalised runtime versus SDC iteration count for the hydrogen flame mechanism. The slope is linear to account for the fact that each SDC iteration adds essentially the same amount of additional work.

5.1. *Computational costs*

We now comment on the computational costs associated with the algorithm. Firstly, the chemical integration step is completely dependent on the stiffness and complexity of the mechanisms, as well as the percentage of the domain covered by the flame front, so we can make no general comparison of chemistry cost to other parts of the algorithm. Similarly, the transport libraries and costs for transport coefficients are problem specific. The linear solves associated with the MAC projection, cell-centred velocity projection, species/enthalpy diffusion solves, and viscous solve use standard multigrid techniques with Gauss–Seidel relaxation. Typically, the multigrid solvers require between 6 and 12 V-cycle iterations to reduce the norm of the residual by a factor of $\sim 10^{12}$. The advection step is a relatively low-cost stencil operation, and is very low cost compared to the linear solves. We note that each SDC iteration can add considerable computational costs, requiring an additional MAC projection, a set of diffusion solves for species and enthalpy, and a chemical integration step with each additional iteration. In Figure 1, we show the normalised runtime as a function of the number of SDC iterations for the hydrogen flame mechanism described in Section 6. In this particular example, the increase in runtime is linear, as expected, and for this mechanism an additional SDC iteration adds $\sim$35% additional runtime as compared to the two-iterations case. The slope of this curve is linear to account for the fact that each SDC iteration adds essentially the same amount of work. We wish to keep the SDC iteration count as low a reasonably possible while balancing error and thermodynamic consistency needs, which we explore in the next section.

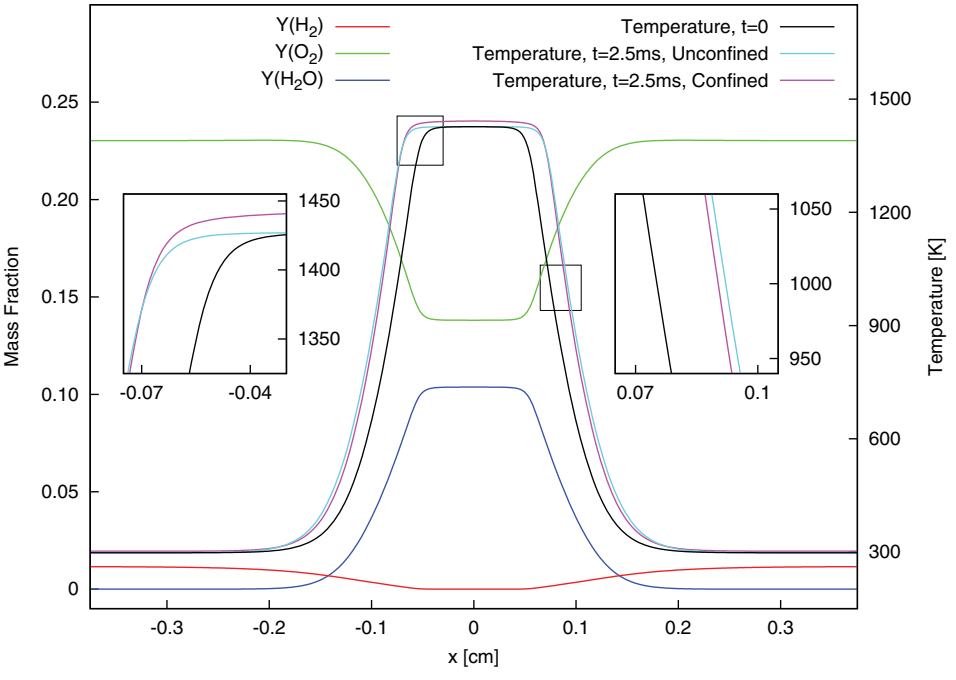

Figure 2. Initial profiles of the primary reactants, product, and temperature for a one-dimensional premixed hydrogen flame. Also shown is the final ($t = 2.5$ ms) temperature profile for the unconfined and confined cases. We highlight two regions of the flame to illustrate the temperature increase in the burned region (left) and the differences in flame front propagation (right) for the confined and unconfined cases. (Colour online)

6. Results

Here we illustrate the behaviour of the new algorithm on several flames. First, we examine the convergence rates and thermodynamic consistency of our algorithm for premixed hydrogen flames in both confined and unconfined domains. Motivated by experiments [37,38], we examine the morphology of thermodiffusively unstable cylindrical hydrogen flames in high-pressure environments for confined and unconfined cases. Next, we compare our algorithm to the previous paper [20] by performing the same premixed methane flame simulations. Finally, we demonstrate that our algorithm is also capable of maintaining the equation of state for non-premixed dimethyl ether jet flames.

6.1. *Convergence test*

For the hydrogen flame simulations we use the H_2/O_2 kinetic model of Burke *et al.* [39]. The initial conditions for the hydrogen flame are obtained by interpolating from a frame-shifted, refined steady 798-point, one-dimensional premixed flame solution computed using the PREMIX code at 10 atm pressure and an equivalence ratio of 0.4. The computational domain has length 0.75 cm. Refer to Figure 2 for the initial configuration of the reactants, products, and temperature, as well as the final temperature profiles for the unconfined and confined cases. We divide the domain into 512, 1024, and 2048 computational cells, and use time steps of $\Delta t = 50$, 25, and 12.5 μs, respectively. These time steps correspond to an advective CFL of $\sigma \sim 0.2$ for the unconfined case, and $\sigma \sim 0.1$ for the confined case (since

Table 1. Error and convergence rates for a premixed hydrogen flame for the unconfined case using two (top), three (middle), and eight (bottom) SDC iterations. The final column shows the percentage error reduction for the $L^1_{1024/2048}$ error as compared to the two-iterations simulation.

Variable	$L^1_{512/1024}$	r	$L^1_{1024/2048}$	Error reduction (%)
$Y(H)$	4.48E−17	1.81	1.28E−17	
$Y(H_2)$	9.50E−14	3.13	1.08E−14	
$Y(O)$	2.24E−15	1.92	5.91E−16	
$Y(OH)$	2.15E−14	2.06	5.16E−15	
$Y(H_2O)$	1.17E−12	2.40	2.22E−13	
$Y(O_2)$	1.13E−12	2.33	2.25E−13	
$Y(HO_2)$	8.52E−15	2.05	2.05E−15	
$Y(H_2O_2)$	7.42E−15	2.16	1.66E−15	
$Y(N_2)$	1.71E−13	2.88	2.32E−14	
ρ	4.75E−11	2.20	1.03E−11	
h	4.76E−06	2.24	1.00E−06	
T	1.26E−08	2.23	2.68E−09	
U	4.90E−11	2.15	1.11E−11	
$Y(H)$	3.47E−17	1.88	9.40E−18	26.5
$Y(H_2)$	8.25E−14	2.77	1.21E−14	−11.8
$Y(O)$	1.64E−15	2.03	4.00E−16	32.4
$Y(OH)$	1.27E−14	2.33	2.52E−15	51.1
$Y(H_2O)$	9.82E−13	2.62	1.60E−13	27.8
$Y(O_2)$	9.23E−13	2.62	1.50E−13	33.3
$Y(HO_2)$	3.49E−15	1.45	1.28E−15	37.7
$Y(H_2O_2)$	5.35E−15	2.15	1.20E-15	27.4
$Y(N_2)$	1.31E−13	2.61	2.15E−14	7.3
ρ	4.25E−11	2.36	8.26E−12	20.0
h	3.76E−06	2.22	8.08E−07	19.5
T	1.05E−08	2.44	1.93E−09	28.2
U	4.73E−11	2.09	1.11E−11	−0.4
$Y(H)$	2.44E−17	1.99	6.15E−18	52.0
$Y(H_2)$	3.57E−14	2.14	8.13E−15	24.9
$Y(O)$	1.07E−15	2.05	2.59E−16	56.3
$Y(OH)$	7.53E−15	2.03	1.85E−15	64.2
$Y(H_2O)$	6.82E−13	1.89	1.85E−13	16.8
$Y(O_2)$	6.92E−13	1.97	1.76E−13	21.5
$Y(HO_2)$	4.98E−15	1.86	1.37E−15	33.1
$Y(H_2O_2)$	3.14E−15	1.87	8.57E−16	48.3
$Y(N_2)$	9.29E−14	1.62	3.02E−14	−30.2
ρ	2.57E−11	2.08	6.08E−12	41.1
h	2.13E−06	1.86	5.85E−07	41.7
T	7.94E−09	1.89	2.14E−09	20.2
U	4.28E−11	2.03	1.05E−11	5.3

the maximum velocity is smaller). We evolve the flame for 2.5 ms to allow the initial data to relax on the coarse grid, and allow the flame to propagate a non-trivial distance through the domain. We perform each simulation using two, three, four, and eight SDC iterations for both the unconfined and confined cases. For the confined case, we use adiabatic, no-slip boundary conditions. As seen in Figure 2, for the confined case the flame propagates more slowly with an increased temperature in the burned region; we will explore this in more detail in our two-dimensional calculations.

In Tables 1 and 2 we report convergence rates for the unconfined and confined simulations for velocity and key thermodynamic variables based on the L_1 norm of errors over the

Table 2. Error and convergence rates for a premixed hydrogen flame for the confined case using two (top), three (middle), and eight (bottom) SDC iterations. Here we also include the time-dependent ambient pressure. The final column shows the percentage error reduction for the $L^1_{1024/2048}$ error as compared to the two-iterations simulation.

Variable	$L^1_{512/1024}$	r	$L^1_{1024/2048}$	Error reduction (%)
$Y(H)$	4.64E−17	1.79	1.34E−17	
$Y(H_2)$	7.92E−14	2.85	1.10E−14	
$Y(O)$	2.34E−15	1.89	6.30E−16	
$Y(OH)$	2.40E−14	2.02	5.92E−15	
$Y(H_2O)$	1.11E−12	2.20	2.42E−13	
$Y(O_2)$	1.18E−12	2.25	2.46E−13	
$Y(HO_2)$	9.36E−15	2.14	2.12E−15	
$Y(H_2O_2)$	7.37E−15	2.11	1.70E−15	
$Y(N_2)$	1.73E−13	2.83	2.43E−14	
ρ	6.11E−11	2.29	1.25E−11	
h	5.00E−06	2.24	1.06E−06	
T	1.31E−08	2.18	2.91E−09	
U	2.26E−11	2.14	5.14E−12	
p_0	1.27E+01	3.19	1.40E+00	
$Y(H)$	3.57E−17	1.85	9.91E−18	26.1
$Y(H_2)$	6.73E−14	2.79	9.75E−15	11.2
$Y(O)$	1.73E−15	2.00	4.31E−16	31.7
$Y(OH)$	1.44E−14	2.29	2.95E−15	50.3
$Y(H_2O)$	8.93E−13	2.46	1.62E−13	32.7
$Y(O_2)$	8.47E−13	2.42	1.58E−13	35.7
$Y(HO_2)$	3.69E−15	1.47	1.33E−15	37.2
$Y(H_2O_2)$	5.31E−15	2.14	1.20E−15	29.2
$Y(N_2)$	1.27E−13	2.58	2.13E−14	12.4
ρ	5.53E−11	2.40	1.05E−11	16.1
h	4.08E−06	2.17	9.08E−07	14.2
T	9.60E−09	2.23	2.05E−09	29.5
U	2.17E−11	2.07	5.16E−12	−0.3
p_0	1.28E+01	2.76	1.90E+00	−36.1
$Y(H)$	2.60E−17	1.99	6.57E−18	51.0
$Y(H_2)$	3.38E−14	2.06	8.13E−15	26.0
$Y(O)$	1.17E−15	2.05	2.82E−16	55.2
$Y(OH)$	8.88E−15	2.02	2.20E−15	62.9
$Y(H_2O)$	7.19E−13	1.85	1.99E−13	17.4
$Y(O_2)$	7.36E−13	1.93	1.93E−13	21.7
$Y(HO_2)$	5.20E−15	1.82	1.48E−15	30.4
$Y(H_2O_2)$	3.19E−15	1.86	8.76E−16	48.5
$Y(N_2)$	9.79E−14	1.63	3.15E−14	−29.5
ρ	2.78E−11	1.91	7.40E−12	40.7
h	2.28E−06	1.85	6.31E−07	40.3
T	8.49E−09	1.86	2.34E−09	19.5
U	1.99E−11	2.01	4.93E−12	4.0
p_0	3.82E+00	2.02	9.43E−01	32.5

entire domain. In each table we report results using two, three, and eight SDC iterations. For the confined case, we also include the convergence rate of the time-evolving ambient pressure, which rises from 10 to approximately 10.6 atm in the course of this simulation (for the ambient pressure, we report the convergence rate of the absolute difference between the final-time values between the coarse-to-medium simulations and the medium-to-fine simulations). We see that, using two SDC iterations, the algorithm obtains second-order

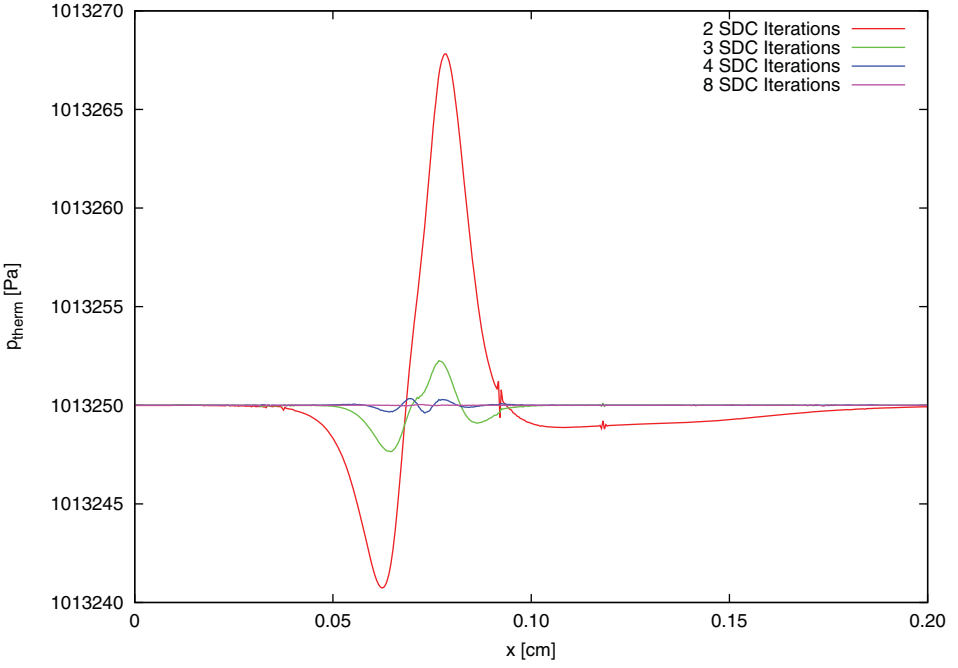

Figure 3. Thermodynamic pressure for the unconfined 2048 zone case at the final time using two, three, four, and eight SDC iterations. As the number of SDC iterations increases, the thermodynamic drift is greatly reduced. (Colour online)

convergence in each variable. As the number of SDC iterations increases, the order of accuracy of the method does not improve, however the L_1 norm of the errors in each variable tends to improve. The last column in these tables shows the percentage error reduction for the $L^1_{1024/2048}$ error as compared to the two-iterations simulation. We observe that the error using three iterations is on average ∼24% smaller than the two-iterations simulations, and the error using eight iterations is on average ∼30% smaller than the two-iterations simulations. This is expected since additional SDC iterations are designed to decrease the splitting error between physical processes [26,27].

6.2. *Thermodynamic consistency*

Using the same setup from the convergence test, we demonstrate that additional SDC iterations decrease the thermodynamic drift. In Figures 3 and 4, we show the effect of increasing the number of SDC iterations on the thermodynamic drift at the final time for the 2048 zone simulation. We observe a significant decrease in drift with each iteration. For the unconfined case, the L_1 (and L_∞) norm of the drift decreases by a factor of 9.0 (7.6) when increasing the iterations from two to three, and then decreases by another factor of 7.1 (6.1) when increasing the iterations from three to four. By eight iterations, the maximum drift is 0.05 Pa. For the confined case, the L_1 (and L_∞) norm of the drift decreases by a factor of 8.8 (7.5) when increasing the iterations from two to three, and then decreases by another factor of 6.0 (4.8) when increasing the iterations from three to four. By eight iterations, the maximum drift is 0.06 Pa. We observe that, with more than eight iterations, the maximum drift remains approximately 0.01 Pa, with a non-oscillatory random pattern. We

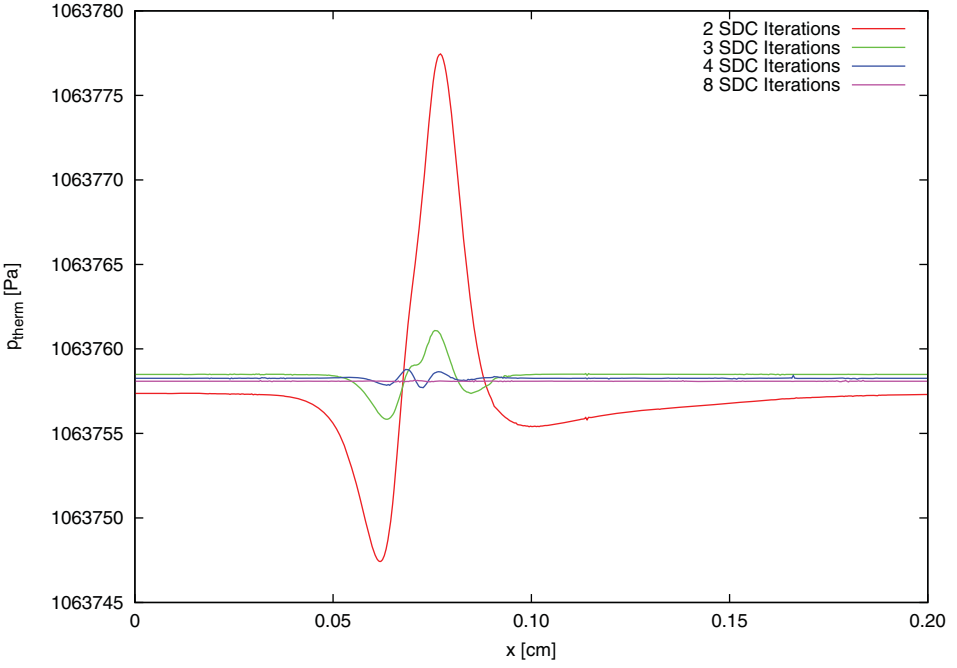

Figure 4. Thermodynamic pressure for the confined 2048 zone case at the final time using two, three, four, and eight SDC iterations. We note that the algorithm is able to capture the ∼5% rise in ambient pressure while simultaneously reducing the thermodynamic drift with increasing iteration count. (Colour online)

conclude that two SDC iterations are sufficient for second-order accuracy; however, there are still gains to be made from performing additional SDC iterations from a thermodynamic consistency standpoint.

6.2.1. *Relaxation parameter*

We also consider the effect of a relaxation parameter, f, on the pressure discrepancy correction:

$$\chi := \chi + \frac{f}{p_{\text{therm}}^{(k)}} \frac{p_{\text{therm}}^{(k)} - p_0}{\Delta t}. \tag{42}$$

In Figure 5 we show the effect of varying f for the finest simulation using three SDC iterations. The choice of $f = 1$ leads to the smallest drift among the tested values. Note that for reported values with $f > 1$, the sign of the thermodynamic drift is opposite from that for reported values with $f < 1$, which is consistent with the idea that $f > 1$ represents an over-relaxation of the correction. We point out that, for this configuration, using $f = 1.1$ (not pictured) decreases the drift even further than $f = 1$, as one might expect looking at the trend in the figure. However, further testing reveals that, depending on the resolution, flame configuration, time step, number of SDC iterations, etc., often using $f = 1$ leads to better results than $f = 1.1$. We conclude that the exact value of f to minimise the drift varies depending on the problem, but in general $f = 1$ is a very reasonable choice.

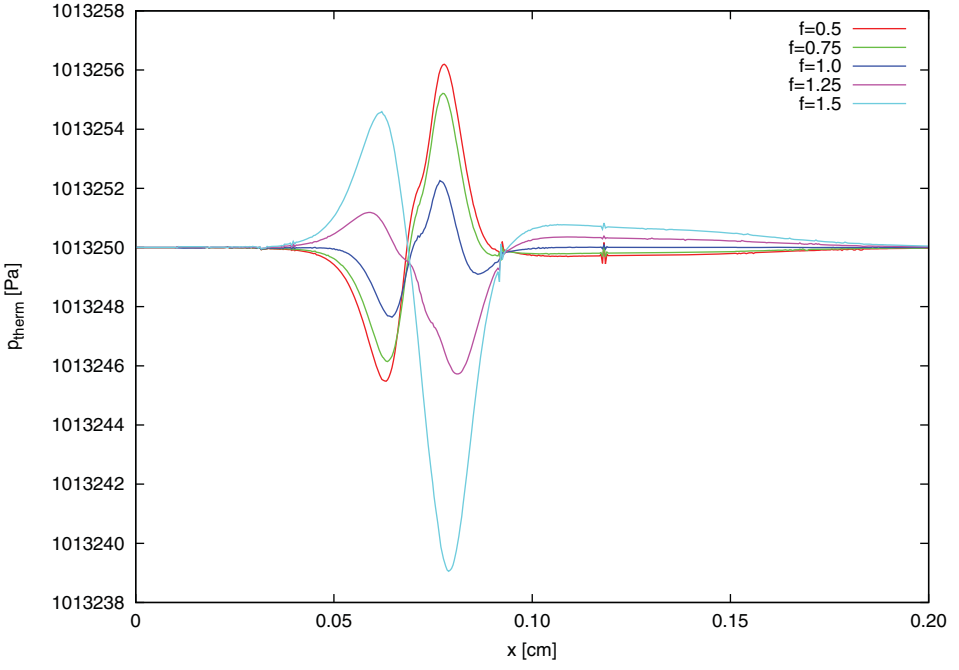

Figure 5. Thermodynamic pressure for the unconfined, 2048 zone case at the final time using $f = 0.5$, 0.75, 1.0, 1.25, and 1.5. Three SDC iterations were used. (Colour online)

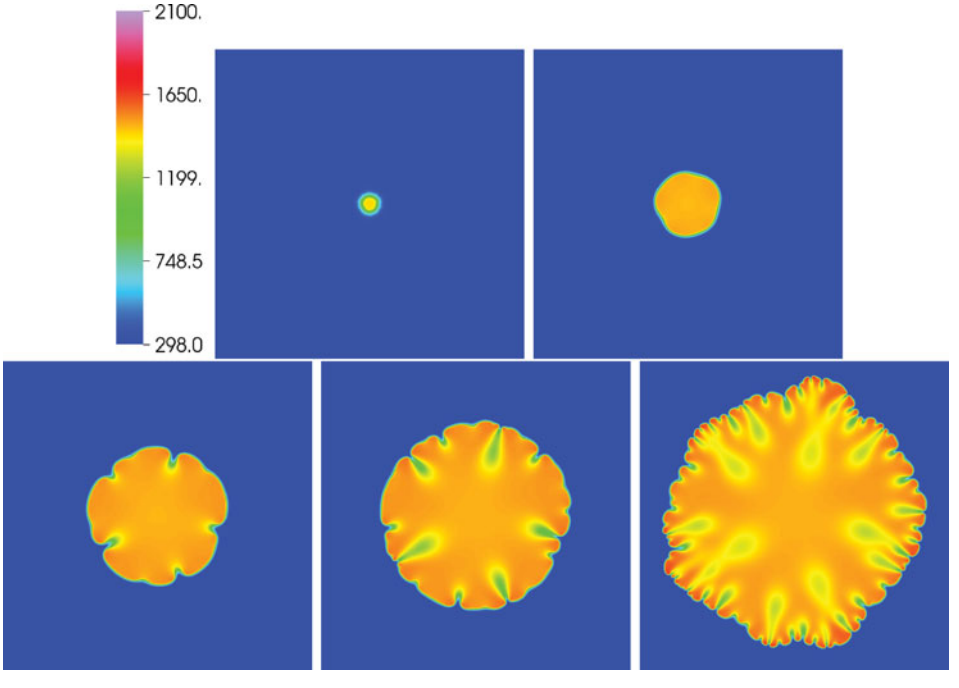

Figure 6. Temperature profiles of an unconfined premixed hydrogen flame at $t = 0$, 20, 40, 50, and 60 ms. Comparing directly to the first five frames in Figure 7, we see that the size of the burned region is noticeably larger. (Colour online)

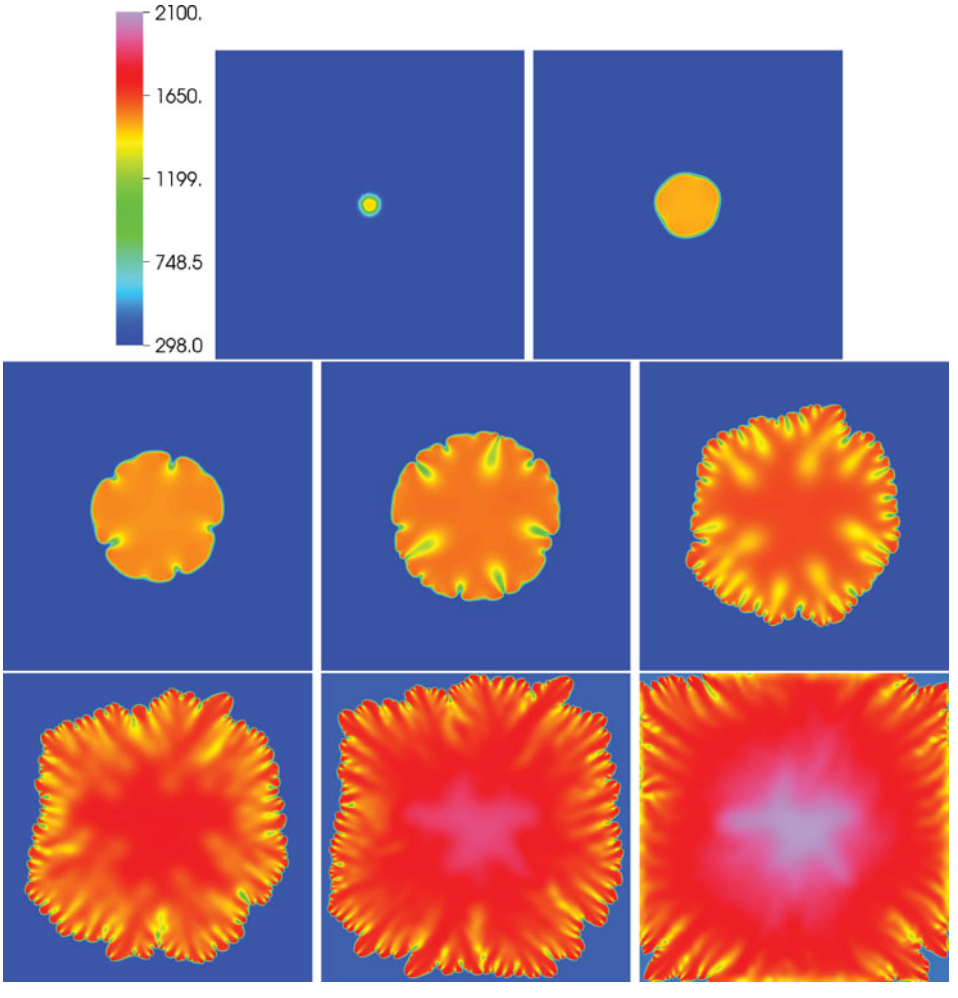

Figure 7. Temperature profiles of a confined premixed hydrogen flame at $t = 0$, 20, 40, 50, 60, 70, 80, and 100 ms. (Colour online)

6.3. *Cylindrical flames*

We now perform more detailed calculations of the surface morphology of thermodiffusively unstable cylindrical hydrogen flames in high-pressure environments. Our simulations are based on studies in [37,38]. We defer more detailed, three-dimensional, AMR simulations to our next paper, where we describe the modifications required to perform AMR. Here we perform confined and unconfined simulations and compare the results.

The two-dimensional simulation domain is 3 cm square with 2048^2 computational zones. Thus our spatial resolution matches the coarsest resolution used in the convergence study above. We use the same PREMIX solution used in the convergence study to initialise the domain, and radially map the solution with an angle-dependent three-mode sinusoidal perturbation. The time step changes over the simulation so that in each step it respects an advective CFL number of $\sigma = 0.2$, so a typical time step is $\sim 20\mu$s, noting that the flame accelerates over time. We use three SDC iterations to control the thermodynamic drift.

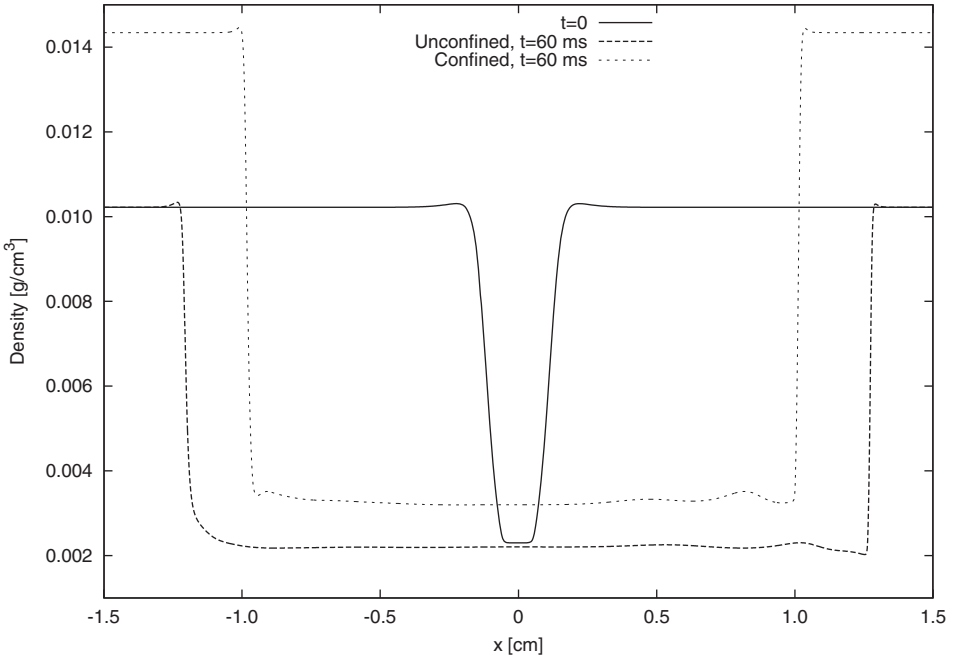

Figure 8. Horizontal profiles of density in the initial configuration, and at $t = 60\,\mathrm{ms}$ for the unconfined and confined cases.

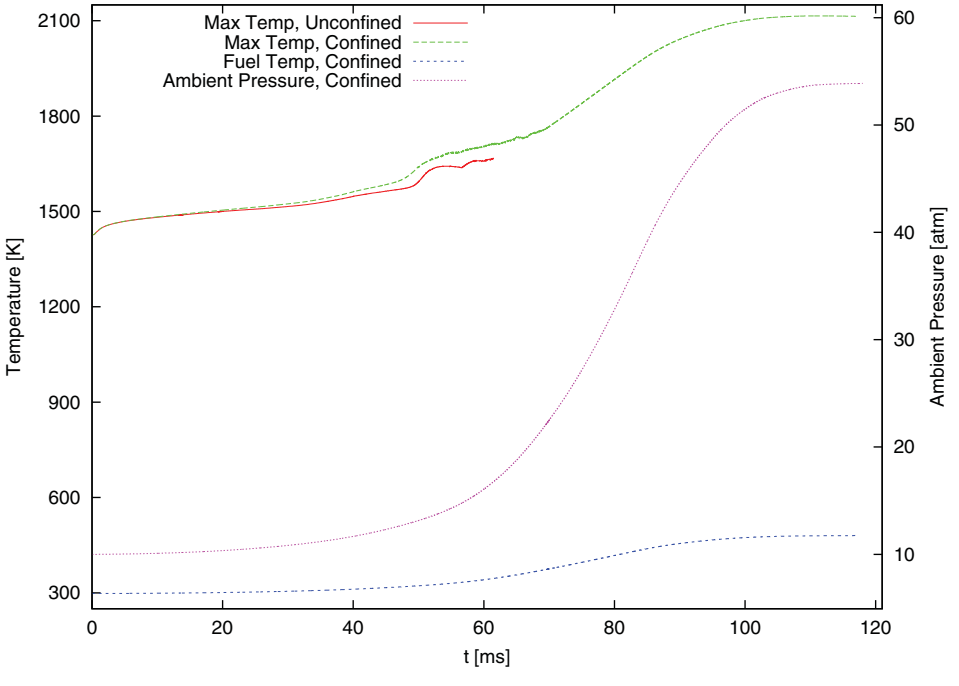

Figure 9. Maximum temperature as a function of time for the unconfined and confined cases. We also show the temperature of the fuel and the ambient pressure for the confined case as a function of time. (Colour online)

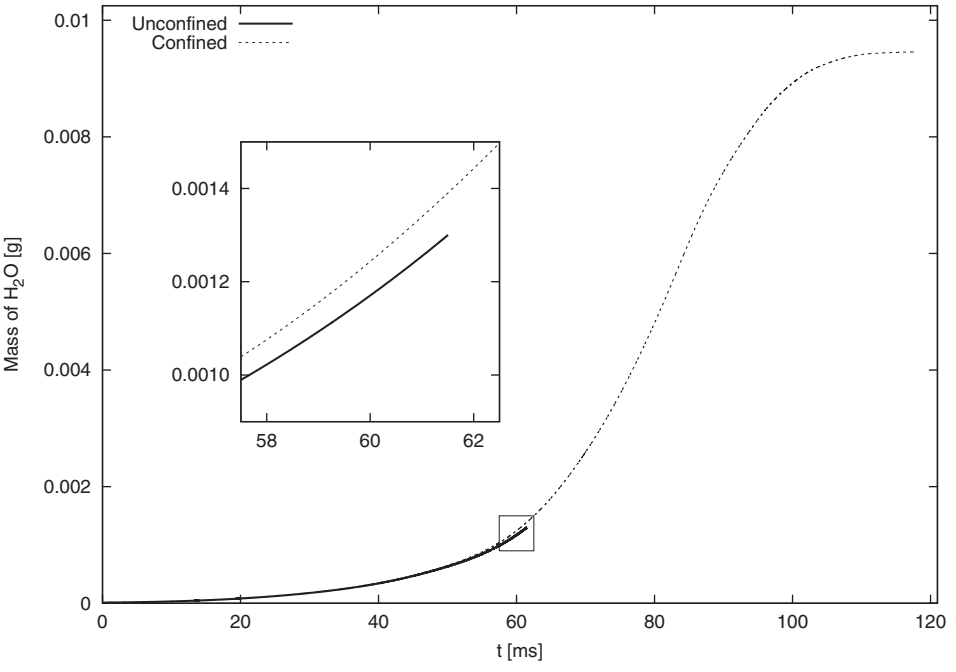

Figure 10. Mass of product as a function of time for the confined and unconfined cases.

In Figures 6 and 7 we show temperature profiles of the initial configuration, as well as profiles at $t = 20$, 40, 50, and 60 ms (for both cases), as well as $t = 70$, 80 and 100 ms for the confined case. We halt the open domain simulation shortly after $t = 60$ ms since the flame front passes through the domain boundary. We note that, for the first 50 ms, the flame morphology looks qualitatively very similar. By 60 ms, the unconfined flame has expanded to a noticeably larger fraction of the domain. This can be more clearly seen in Figure 8, which shows a horizontal profile of the density field about the centre of the domain in the initial data, and at $t = 60$ ms.

We see in the confined case that, by $t = 100$ ms, the flame has expanded to cover nearly the entire computational domain, and the maximum temperature in the burnt region has increased from ∼1400 K (at $t = 0$), to ∼1700 K (at $t = 60$ ms), to ∼2100 K (at $t = 100$ ms). In Figure 9, we plot the maximum temperature as a function of time for both simulations, as well as the fuel temperature for the confined case, which rises from 298 to 475 K over the course of the simulation due to the ambient pressure and fuel density increase. Also included in Figure 9 is a plot of the ambient pressure as a function of time for the confined case, which rises from 10 to 54 atm.

In Figure 10 we plot the mass of H_2O product as a function of time for both simulations. Despite the difference in the size of the burnt region at $t = 60$ ms, the amount of H_2O is very similar, as seen in the figure inset. At $t = 60$ ms, the confined simulation has produced 6.2% more H_2O than the unconfined case. At earlier times, the amount of H_2O produced is (relatively) closer, with a 1.9% difference at $t = 40$ ms and a 0.7% difference at $t = 20$ ms.

Next we examine the effects of increasing SDC iterations for the unconfined case. In Figure 11 we examine the thermodynamic drift from the unconfined simulation depicted in Figure 6 at $t = 40$ ms using two, three, and eight SDC iterations. By examining the maximum

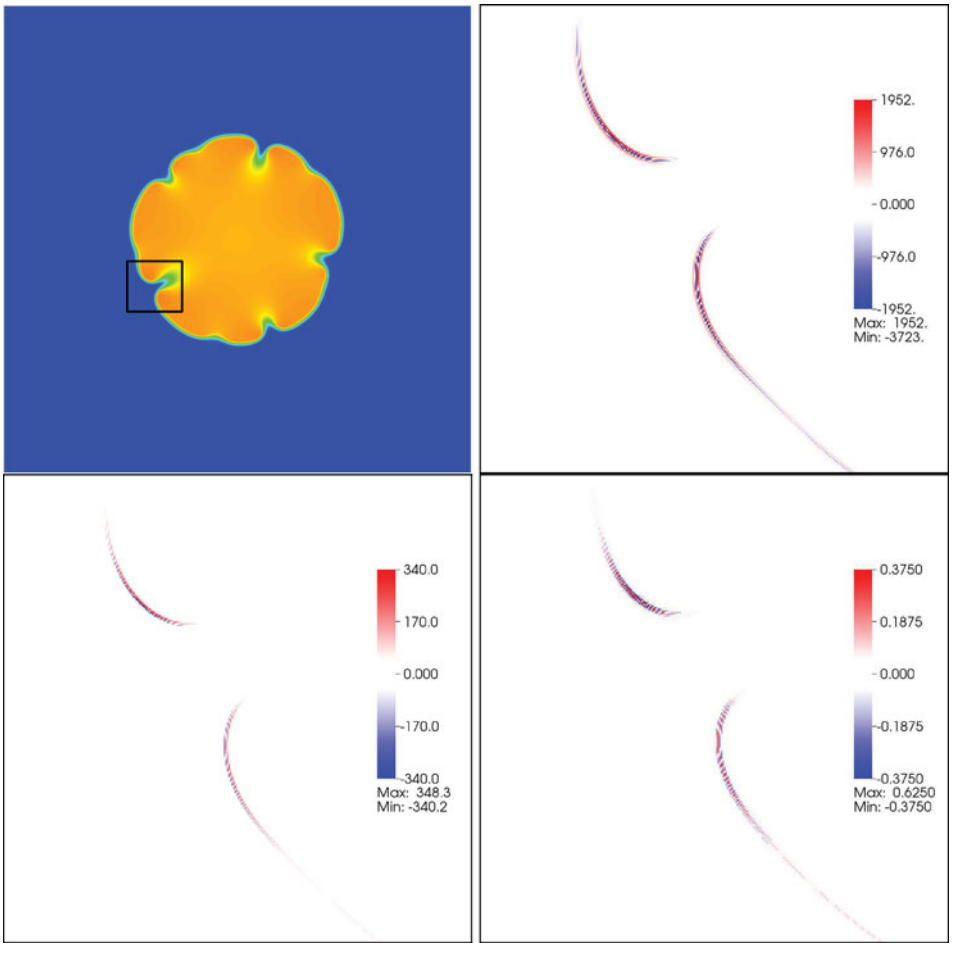

Figure 11. Temperature configuration for the cylindrical hydrogen flame at $t = 40$ ms (this is the same image and colour scale used in Figure 6). The other panels show the thermodynamic drift ($p_{\text{therm}} - p_0$) as a function of the number of SDC iterations in the region indicated in the top-left panel; (top-right) two iterations; (bottom-left) three iterations; (bottom-right) eight iterations. Note that the global maxima and minima are reported, and each simulation has a different colour scale. (Colour online)

and minimum drift indicated in the legends, we can clearly see that the additional SDC iterations greatly reduce the drift.

To look more closely at the effect of increasing SDC iterations, we perform additional unconfined simulations as before, but with twice the spatial resolution and an advective CFL of 0.1. We perform simulations using three, four, five, six, seven, and eight SDC iterations and examine the amount of product (H_2O). In Figure 12 we show the amount of product as a function of time at $t \sim 5$ ms for each iteration count. The absolute difference in H_2O is relatively small, yet we can clearly see that, as the iteration count increases, the amount of product is converging.

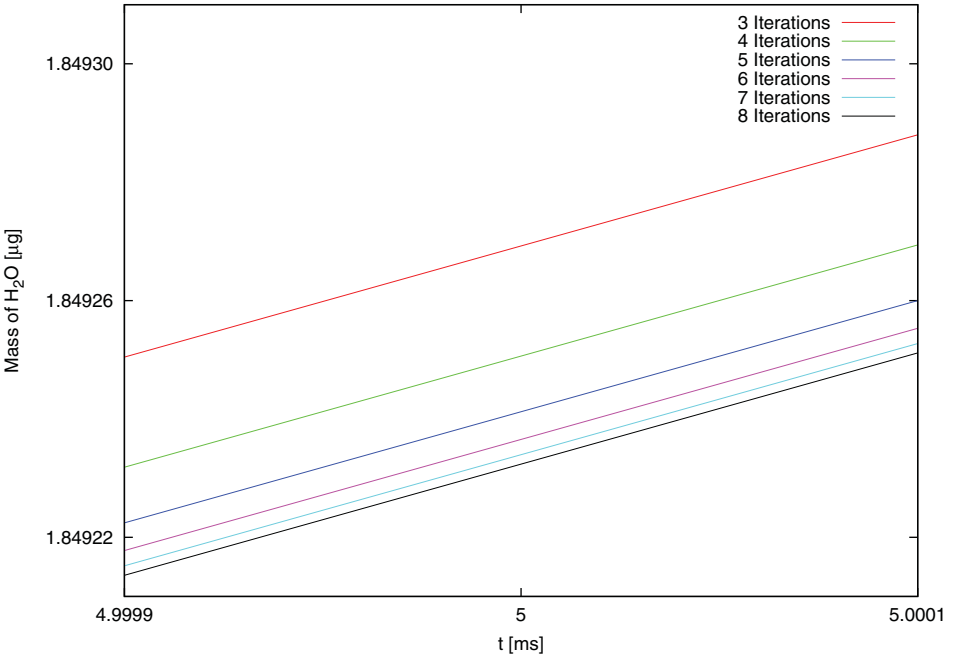

Figure 12. The amount of product as a function of time for the cylindrical hydrogen flame for increasing SDC iteration counts. The amount of product is clearly converging as the iteration count increases. (Colour online)

6.4. *Comparison to previous algorithm*

We now demonstrate the improvement in thermodynamic drift compared to the previous algorithm in [20]. We repeat the 1 atm methane flame example (GRIMech-3.0; 53 species, 325-step network [40]) from Section 5.1 in [20] using exactly the same setup to simulate a one-dimensional unconfined premixed flame. We use the finest resolution case (1.2 cm domain, 2048 grid cells, $\Delta t = 1.5625\,\mu$s) and compare the drift after 10 time steps and after 320 time steps to our new algorithm with both two and three SDC iterations. Figure 13 shows a comparison of the thermodynamic pressure for each algorithm at the early and later times. At early times, our new algorithm has a much smaller drift that the previous algorithm, which further improves with additional SDC iterations. At later times, the previous algorithm has reduced drift as well, and is comparable to the new algorithm with two SDC iterations. However, our new algorithm with additional SDC iterations greatly reduces the drift drift, as expected. We note that the computational cost of the previous algorithm nearly matches the cost of the new algorithm with two SDC iterations, except that there is one additional linear solve for the MAC projection in the new algorithm. For large networks, this additional cost is essentially negligible due to the large number of diffusion linear solves.

6.5. *Non-premixed dimethyl ether jet*

As a final test of our code, we perform two-dimensional simulations of a 39-species non-premixed dimethyl ether (DME) jet flame. The simulation parameters exactly match those described in Section 5.3 of [41], except the simulations use 1024^2 grid cells instead of

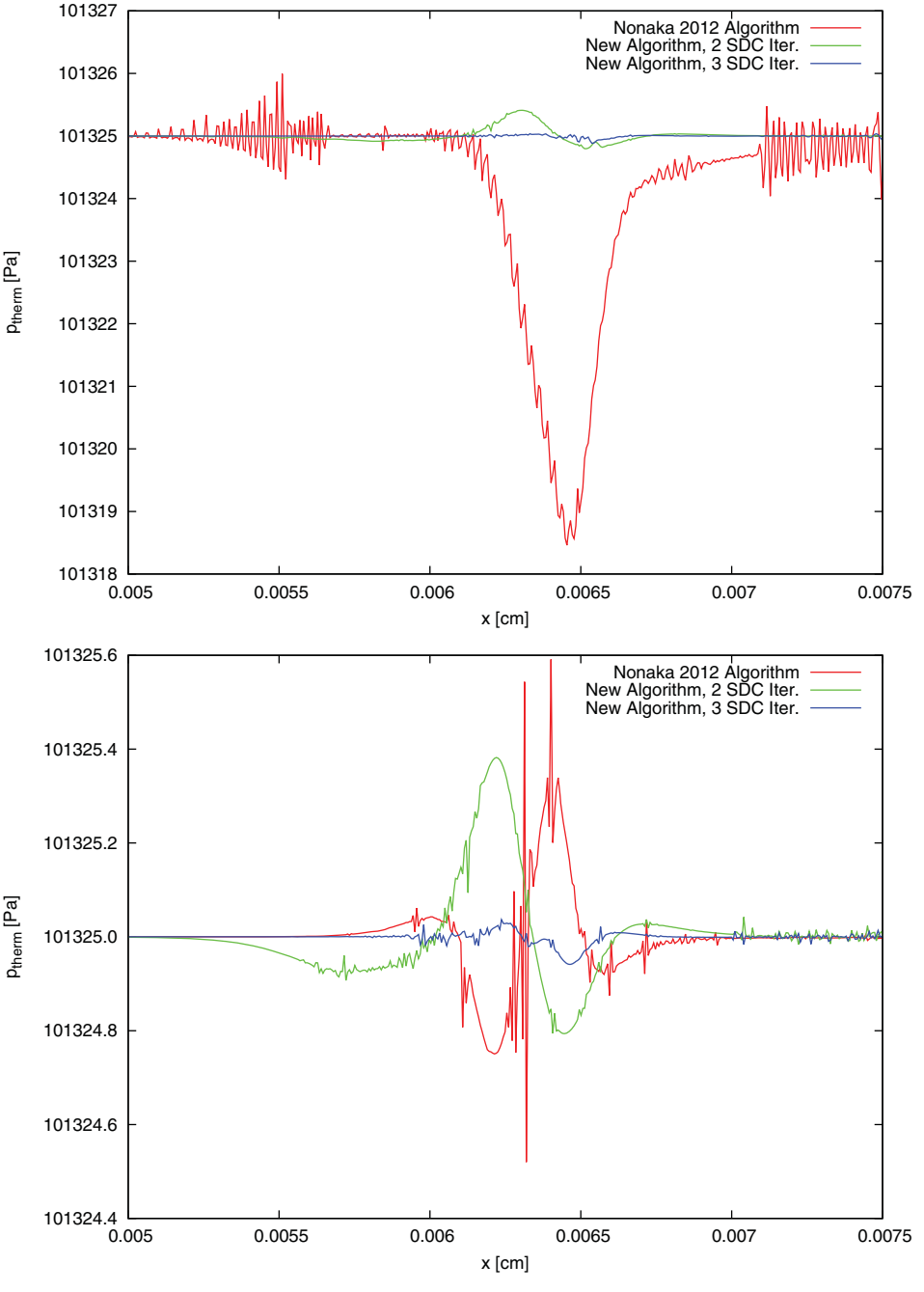

Figure 13. Thermodynamic pressure for an unconfined premixed 1 atm methane flame using the previous algorithm from [20] and the new algorithm using two and three SDC iterations. We used the same test as in Section 5.1 of [20], running the finest resolution case for (top) 10 time steps and (bottom) 320 time steps. (Colour online)

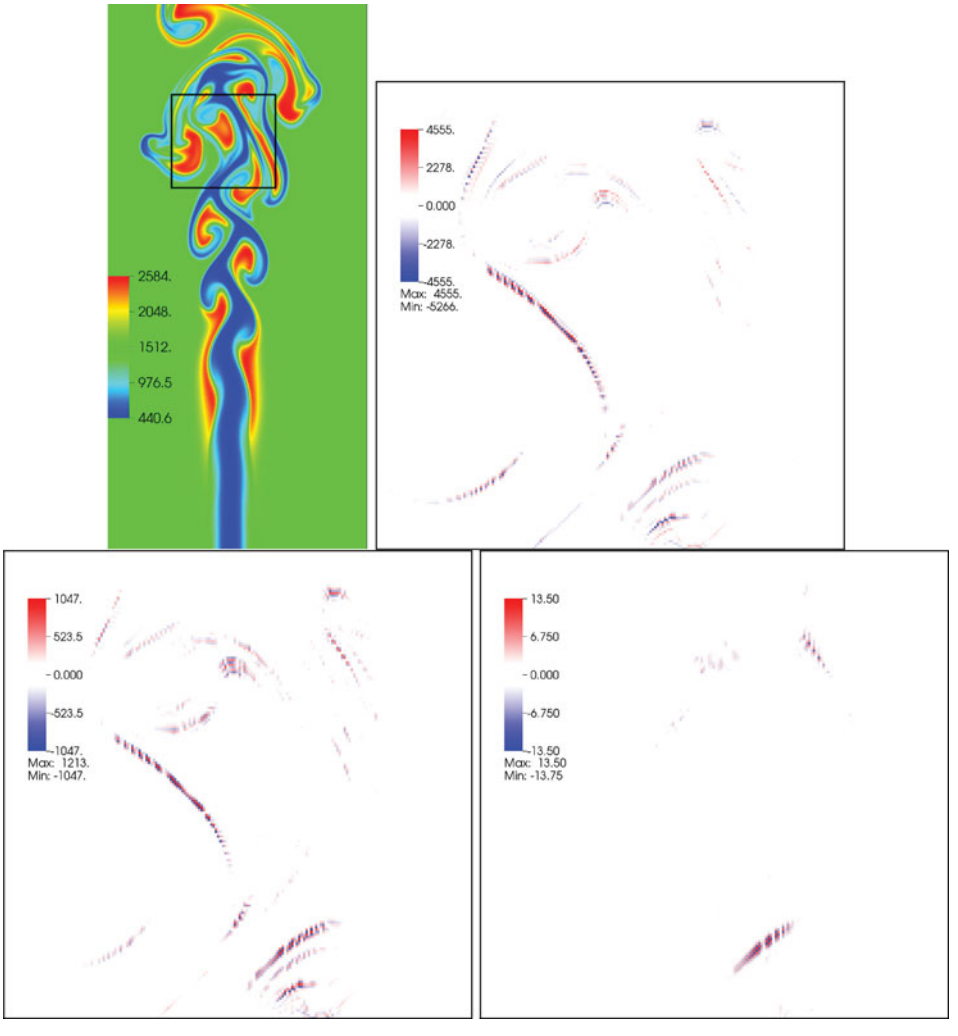

Figure 14. Top-left: temperature configuration for the non-premixed dimethyl ether jet flame at $t = 60\,\mu$s. The other panels show the thermodynamic drift ($p_{\text{therm}} - p_0$) as a function of the number of SDC iterations in the region indicated in the top-left panel; (top-right) two iterations; (bottom-left) three iterations; (bottom-right) eight iterations. Note that the global maxima and minima are reported, and each simulation has a different colour scale. (Colour online)

2048^2 grid cells. We use an advective CFL of 0.7 to simulate to $60\,\mu$s (the average time step is $\sim$30 ns on an $L = 0.228$ cm domain). In Figure 14 we show the the final temperature profile in the central part of the domain and insets of the thermodynamic drift for two, three, and eight SDC iterations. Similar to the cylindrical hydrogen flames, we see a great improvement in the thermodynamic drift as the iterations increase.

7. Conclusions

We have developed an iterative scheme for evolving thermodynamic variables in a fully conservative manner while staying consistent with the EOS. The method naturally fits

into an iterative SDC methodology. We have also developed a model for handling ambient pressure changes in confined domains. We have shown that two SDC iterations are sufficient for second-order accuracy, and that additional iterations greatly reduce the thermodynamic drift. We have also shown that our methodology is useful for studying multi-dimensional flames under realistic experimental conditions.

In the next paper we will extend our simulation methodology to utilise AMR. There are at least three issues associated with AMR. First, we need to re-factor the algorithm to use the net fluxes of mass, energy, and momentum when posed in an SDC correction form in the mulitlevel synchronisation steps, as opposed to using the net fluxes in the Strang splitting formulation used in [19]. Second, in the original AMR approach, the multilevel synchronisation steps did nothing to ensure that the solution either stayed on, or was driven toward, the EOS. We can implement an iterative pressure discrepancy algorithm in the multilevel synchronisation steps to reduce the drift everywhere, but particularly near the coarse–fine interface where synchronising the coarse and fine fluxes often causes numerical drift. Third, we need to develop a methodology for advancing and synchronising the ambient pressure across levels of refinement in a subcycling adaptive framework. There is a question about how to represent the trajectory of p_0 over time, given that the different AMR levels are advanced, typically, at different time steps, and how to form synchronisation equations that drive the solution toward the constraint while correcting p_0. In future work, we also plan to extend this algorithm to more general equations of state, which will allow improved fidelity simulations at high pressure. This includes nuclear flames in an astrophysical setting; we would like to examine the performance of the pressure discrepancy approach using our `MAESTRO` astrophysical code framework [11].

Disclosure statement

No potential conflict of interest was reported by the authors.

Funding

Work at the Lawrence Berkeley National Laboratory was supported by the Applied Mathematics Program of the Department of Energy (DOE) Office of Advanced Scientific Computing Research under US DOE contract [DE-AC02-05CH11231].

References

[1] H.N. Najm, M. Valorani, D.A. Goussis, and J. Prager, *Analysis of methane–air edge flame structure*, Combust. Theory Model. 14 (2010), pp. 257–294.

[2] J. Prager, H.N. Najm, M. Valorani, and D. Goussis, *Structure of n-heptane/air triple flames in partially-premixed mixing layers*, Combust. Flame 158 (2011), pp. 2128–2144.

[3] Z. Wang, E. Motheau, and J. Abraham, *Effects of equivalence ratio variations on turbulent flame speed in lean methane/air mixtures under lean-burn natural gas engine operating conditions*, Proc. Combust. Inst. 36 (2016), pp. 3423–3430. https://www.researchgate.net/publication/309193168_Effects_of_equivalence_ratio_variations_on_turbulent_flame_speed_in_lean_methaneair_mixtures_under_lean-burn_natural_gas_engine_operating_conditions

[4] A. Aspden, M. Day, and J. Bell, *Turbulence–chemistry interaction in lean premixed hydrogen combustion*, Proc. Combust. Inst. 35 (2015), pp. 1321–1329.

[5] A. Aspden, J. Bell, M. Day, and F. Egolfopoulos, *Turbulence–flame interactions in lean premixed dodecane flames*, Proc. Combust. Inst. (2016), pp. 1–8.

[6] A. Aspden, M. Day, and J. Bell, *Three-dimensional direct numerical simulation of turbulent lean premixed methane combustion with detailed kinetics*, Combust. Flame 166 (2016), pp. 266–283.

[7] M. Day, S. Tachibana, J. Bell, M. Lijewski, V. Beckner, and R.K. Cheng, *A combined computational and experimental characterization of lean premixed turbulent low swirl laboratory flames. Part I: Methane flames*, Combust. Flame 159 (2012), pp. 275–290.

[8] M. Day, S. Tachibana, J. Bell, M. Lijewski, V. Beckner, and R.K. Cheng, *A combined computational and experimental characterization of lean premixed turbulent low swirl laboratory flames. Part II: Hydrogen flames*, Combust. Flame 162 (2015), pp. 2148–2165.

[9] R.G. Rehm and H.R. Baum, *The equations of motion for thermally driven buoyant flows*, J. Res. Nat. Bur. Stand. 83 (1978), pp. 297–308.

[10] A. Majda and J.A. Sethian, *Derivation and numerical solution of the equations of low Mach number combustion*, Combust. Sci. Technol. 42 (1985), pp. 185–205.

[11] A. Nonaka, A.S. Almgren, J.B. Bell, M.J. Lijewski, C.M. Malone, and M. Zingale, *MAESTRO: An adaptive low Mach number hydrodynamics algorithm for stellar flows*, Astrophys. J. Suppl. 188 (2010), pp. 358–383. paper V. https://ccse.lbl.gov/Research/MAESTRO/AASposter2010.pdf

[12] M. Duarte, A.S. Almgren, and J.B. Bell, *A low Mach number model for moist atmospheric flows*, J. Atmosph. Sci. 72 (2015), pp. 1605–1620.

[13] H.N. Najm, P.S. Wyckoff, and O.M. Knio, *A semi-implicit numerical scheme for reacting flow. Part I: Stiff chemistry*, J. Comput. Phys. 143 (1998), pp. 381–402.

[14] O.M. Knio, H.N. Najm, and P.S. Wyckoff, *A semi-implicit numerical scheme for reacting flow. Part II: Stiff, operator-split formulation*, J. Comput. Phys. 154 (1999), pp. 428–467.

[15] H.N. Najm and O.M. Knio, *Modeling low Mach number reacting flow with detailed chemistry and transport*, J. Sci. Comput. 25 (2005), pp. 263–287.

[16] R. Yu, J. Yu, and X.S. Bai, *An improved high-order scheme for DNS of low Mach number turbulent reacting flows based on stiff chemistry solver*, J. Comput. Phys. 231 (2012), pp. 5504–5521.

[17] C. Safta, J. Ray, and H.N. Najm, *A high-order low-Mach number AMR construction for chemically reacting flows*, J. Comput. Phys. 229 (2010), pp. 9299–9322.

[18] E. Motheau and J. Abraham, *A high-order numerical algorithm for DNS of low-Mach-number reactive flows with detailed chemistry and quasi-spectral accuracy*, J. Comput. Phys. 313 (2016), pp. 430–454.

[19] M.S. Day and J.B. Bell, *Numerical simulation of laminar reacting flows with complex chemistry*, Combust. Theory Model. 4 (2000), pp. 535–556.

[20] A. Nonaka, J.B. Bell, M.S. Day, C. Gilet, A.S. Almgren, and M.L. Minion, *A deferred correction coupling strategy for low Mach number flow with complex chemistry*, Combust. Theory Model. 16 (2012), pp. 1053–1088.

[21] W.E. Pazner, A. Nonaka, J.B. Bell, M.S. Day, and M.L. Minion, *A high-order spectral deferred correction strategy for low Mach number flow with complex chemistry*, Combust. Theory Model. 20 (2016), pp. 521–547. http://dx.doi.org/10.1080/13647830.2016.1150519.

[22] J.B. Bell, P. Colella, and H.M. Glaz, *A second order projection method for the incompressible Navier–Stokes equations*, J. Comput. Phys. 85 (1989), pp. 257–283.

[23] J.B. Bell, P. Colella, and L.H. Howell, *An efficient second-order projection method for viscous incompressible flow*, in *Proceedings of the Tenth AIAA Computational Fluid Dynamics Conference*, 24–27June 1991, Honolulu, HI, AIAA, Reston, VA, pp. 360–367.

[24] A.J. Chorin, *Numerical solution of the Navier–Stokes equations*, Math. Comput. 22 (1968), pp. 745–762.

[25] A. Dutt, L. Greengard, and V. Rokhlin, *Spectral deferred correction methods for ordinary differential equations*, BIT 40 (2000), pp. 241–266.

[26] A. Bourlioux, A.T. Layton, and M.L. Minion, *High-order multi-implicit spectral deferred correction methods for problems of reactive flow*, J. Comput. Phys. 189 (2003), pp. 651–675.

[27] A.T. Layton and M.L. Minion, *Conservative multi-implicit spectral deferred correction methods for reacting gas dynamics*, J. Comput. Phys. 194 (2004), pp. 697–715.

[28] P.N. Brown, G.D. Byrne, and A.C. Hindmarsh, *VODE: A variable coefficient ODE solver*, SIAM J. Sci. Stat. Comput. 10 (1989), pp. 1038–1051.

[29] R.J. Kee, J. Warnatz, and J. Miller, *FORTRAN computer-code package for the evaluation of gas-phase viscosities, conductivities, and diffusion coefficients. [CHEMKIN]*, Tech. Report. SAND83-8209, Sandia National Labs, Livermore, CA, National Technical Information Service (NTIS), US Department of Commerce, Springfield, VA, 1983.

[30] J. Warnatz, *Influence of transport models and boundary conditions on flame structure*, in *Numerical Methods in Laminar Flame Propagation*, Springer Fachmedien, Wiesbaden, Germany, 1982, pp. 87–111. https://doi.org/10.1007/978-3-663-14006-1_8.
[31] A.S. Almgren, J.B. Bell, C.A. Rendleman, and M. Zingale, *Low Mach number modeling of Type Ia supernovae. Part I: Hydrodynamics*, Astrophys. J. 637 (2006), pp. 922–936.
[32] A.S. Almgren, J.B. Bell, P. Colella, L.H. Howell, and M.L. Welcome, *A conservative adaptive projection method for the variable density incompressible Navier–Stokes equations*, J. Comput. Phys. 142 (1998), pp. 1–46.
[33] F.H. Harlow and E. Welch, *Numerical calculation of time-dependent viscous incompressible flow of fluids with free surface*, Phys. Fluids 8 (1965), Article ID 2182. http://dx.doi.org/10.1063/1.1761178.
[34] P. Colella, *Multidimensional upwind methods for hyperbolic conservation laws*, J. Comput. Phys. 87 (1990), pp. 171–200.
[35] J. Saltzman, *An unsplit 3D upwind method for hyperbolic conservation laws*, J. Comput. Phys. 115 (1994), pp. 153–168.
[36] R.B. Pember, L.H. Howell, J.B. Bell, P. Colella, W.Y. Crutchfield, W.A. Fiveland, and J.P. Jessee, *An adaptive projection method for unsteady low-Mach number combustion*, Combust. Sci. Technol. 140 (1998), pp. 123–168.
[37] S. Tse, D. Zhu, and C. Law, *Morphology and burning rates of expanding spherical flames in H_2/O_2/inert mixtures up to 60 atmospheres*, Proc. Combust. Inst. 28 (2000), pp. 1793–1800.
[38] G. Jomaas and C.K. Law, *Surface morphology and self-acceleration of expanding spherical flames*, Presented at the 47th AIAA Aerospace Sciences Meeting including The New Horizons Forum and Aerospace Exposition, 5–8 January 2009, Orlando, FL, Paper AIAA 2009-1185. http://dx.doi.org/10.2514/6.2009-1185.
[39] M.P. Burke, M. Chaos, Y. Ju, F.L. Dryer, and S.J. Klippenstein, *Comprehensive H_2/O_2 kinetic model for high-pressure combustion*, Int. J. Chem. Kinetics 44 (2012), pp. 444–474. http://dx.doi.org/10.1002/kin.20603.
[40] M. Frenklach, H. Wang, M. Goldenberg, G.P. Smith, D.M. Golden, C.T. Bowman, R.K. Hanson, W.C. Gardiner, and V. Lissianski, *GRI-Mech – An optimized detailed chemical reaction mechanism for methane combustion*, Tech. Rep. GRI-95/0058, Gas Research Institute, 1995. http://www.me.berkeley.edu/gri_mech/
[41] M. Emmett, W. Zhang, and J.B. Bell, *High-order algorithms for compressible reacting flow with complex chemistry*, Combust. Theory Model. 18 (2014), pp. 361–387.